

# ACTIVE THERMOGRAPHY USING CELLPHONE ATTACHMENT INFRARED CAMERA

NAKISA SAMADI

A THESIS SUBMITTED TO THE FACULTY OF GRADUATE STUDIES IN  
PARTIAL FULFILLMENT OF THE REQUIREMENTS FOR THE DEGREE OF  
MASTER OF APPLIED SCIENCE

GRADUATE PROGRAM IN MECHANICAL ENGINEERING

YORK UNIVERSITY

TORONTO, ONTARIO

JUNE 2020

©NAKISA SAMADI, 2020

## Abstract

Active thermography (AT) is a widely studied non-destructive testing method for the characterization and evaluation of biological and industrial materials. Despite promising applications of AT in industry and medicine, commercialization and wide-spread adaption of AT has long been impeded by the high cost (usually \$10k-\$100k) and large size of infrared cameras. In order to overcome these limitations, in this thesis, we aim to demonstrate feasibility of performing AT with cell-phone attachment infrared cameras with cost of ~\$250 and size significantly less than the research-grade infrared cameras. This involves developing a hardware-level code/software for controlling camera attributes in order to achieve stable acquisition of frames at high frame rates. Given the importance of portability, we also demonstrate possibility of developing a setting that is both portable and easy to set up. The nominal frame rate of camera through its standard applet is less than 9fps. In order to achieve higher frame rate, we utilized USB 2.0 documentation and Microsoft Windows native application programming interfaces to set up packets of information. These packets of information were then sent to the cameras default endpoint address and, subsequently, acquire frame data from camera through a corresponding pipe.

As such, the developed platform has not only the ability to control camera attributes (e.g., calibrate camera, acquire frame, etc) through a simple USB interface but also can achieve a stable high frame rate of 33fps through a circular buffer hierarchy and multi-threading. To demonstrate performance of developed low-cost and portable system, two series of AT experiments were conducted: (i) in response to the recent legalizations of marijuana in Canada, we interrogated the photothermal responses of commercially available oral fluid lateral flow immunoassays (LFIA) with the developed system. The results of our low-cost setup represent that it can reliably detect THC concentrations as low as 2ng/ml in oral fluid with 95% accuracy. (ii) To demonstrate ability of the system in early detection of dental caries, artificially-induced caries were imaged using the low cost and portable system. Our results suggested the ability of the developed AT low cost system for detecting early dental carries.

## **Acknowledgement**

*This thesis is dedicated to my parents.*

*For their endless love, passion, and encouragement*

## Table of Contents

Abstract.....	ii
Acknowledgement .....	iii
Table of Contents.....	iv
List of Tables .....	vii
List of Figures .....	viii
1. Introduction .....	1
1.1. Active Thermography .....	1
1.2. Lock-in Thermography .....	2
1.3. Theory of Lock-in Thermography.....	3
1.4. Objective and outlook of the Thesis.....	5
1.4.1. Overview of the First Paper .....	6
1.4.2. Overview of the Second Paper.....	7
1.4.3. Overview of the Final Paper .....	8
2. Comparison of Low Cost and Research Grade Active Thermography Platforms for Detection of Early Dental Caries .....	10
2.1. Abstract .....	10
2.2. Introduction .....	10
2.3. Methods.....	12
2.3.1. Dental Sample Preparation .....	12
2.3.2. Lock-in-Thermography: Principles and Instrumentations .....	12
2.4. Results and Discussion.....	14
2.5. Conclusion.....	17
2.6. References .....	17

3. Thermographic Detection and Quantification of THC in Oral Fluid at Unprecedented Low Concentrations .....	19
3.1. Abstract .....	19
3.2. Introduction .....	19
3.3. Methods.....	22
3.3.1. Lateral flow immunoassay .....	22
3.3.2. Preparation of oral fluid-THC solutions and LFA test strips.....	24
3.3.3. Lock-In Thermography Interpretation of LFAs.....	24
3.3.4. Visual Interpretation of LFAs.....	25
3.3.5. Data Analysis .....	26
3.4. Results .....	28
3.4.1. Lock-In Thermography Interpretation of LFAs.....	28
3.4.2. Visual Interpretation of LFAs.....	31
3.5. Discussion and Conclusion .....	31
3.6. References .....	34
4. Low-Cost Active Thermography using Cellphone Infrared Cameras: from Early Detection of Dental Caries to Quantification of THC in Oral Fluid.....	38
4.1. Abstract .....	38
4.2. Introduction .....	39
4.3. Results and Discussions .....	41
4.4. Conclusions .....	55
4.5. Methods.....	56
4.5.1. Principle of Lock-in Thermography (LIT) .....	56
4.6. Supplementary Documents .....	64
4.7. References .....	65
5. Conclusion and Future Work.....	69

5.1. Conclusion.....	69
5.2. Future Work .....	70
6. References .....	72

## List of Tables

Table 3.1. Four possible outcomes: true positive (TP), true negative (TN), false positive (FP), false negative (FN) at different criterion/cut-off levels (i.e., bin numbers).....	27
Table 3.2. Sensitivity, specificity, accuracy, positive predictive value (PPV) and negative predictive value (NPV) calculated from the visual and LIT interpretation of LFAs at various criterion/cut-off. ....	30
Table 4.1 Means and STDs of the probability density functions calculated from the Supplementary Fig. 4.7. ....	63

## List of Figures

Figure 1.1. The operation of Lock-in [22] .....	5
Figure 2.1. (a) Schematic illustration of the experimental set-up of a cellphone-based Lock-in-Thermography.....	13
Figure 2.2. : LIT amplitude (a) and phase (b) images of a dental sample s1 taken by the low-cost LIT system. The corresponding amplitude (c) and phase image (d) from the high-end research grade LIT system .....	16
Figure 2.3. LIT amplitude (a) and phase (b) images of a dental sample s2 taken by the low-cost LIT system. The corresponding amplitude (c) and phase image (d) from the high-end research grade LIT system .....	16
Figure 3.1. (a) Schematic diagram of LFA test strip. Schematic illustration of binding mechanisms of competitive LFAs (b) before use, (c) negative test, and (d) positive test with their respective visual appearance.....	23
Figure 3.2. (a) A schematic diagram of the LIT imaging system used for the interpretation of LFA test strips. (b) Amplitude image after LIT measurement. (c) Average intensity of pixels over all the columns in a strip.....	25
Figure 3.3. (a) Visual and LIT images of 6 representative LFAs at concentrations of 0, 2, 5, 7.5, 10 and 25 ng/ml. (b) Normalized amplitude values obtained from LIT LFA images in (a). (c) Distribution of the entire dataset of the LFAs at various concentrations obtained from the LIT system. (d) Mean normalized amplitude at different THC concentrations obtained from (c) with 99% confidence interval error bars. ....	29
Figure 3.4. Percentage of LFAs of various concentrations dropped in bin number 1-6 in LIT (a) and visual interpretation (b). (c) ROC curves from the visual and LIT interpretation data. ....	30
Figure 4.1. Temporal variations of surface temperature captured by (a) the SEEK THERMAL app and (b) developed SDK. (c) and (d) are Fourier spectrums of (a) and (b), respectively. ....	42
Figure 4.2. (a) Photograph of a thermal heat sink; red dashed rectangle depicts the imaging area. LIT Amplitude image of the area of heat sink imaged at modulation frequency with camera frame rates of (b) 9 fps and (c) 33 fps. (d) LIT Amplitude image at a modulation frequency of 10Hz and camera frame rate of 33 Hz, demonstrating the possibility of resolving small defects with the improved resolution at higher modulation frequencies with high frame rates. ....	42

Figure 4.3(a) A schematic diagram of the cross-section of the block with a blind hole at 300 $\mu$ m, 500 $\mu$ m, and 800 $\mu$ m beneath the interrogated surface. (b1-b3) Amplitude images from 300 $\mu$ m hole obtained from LIT demodulation at camera frame rates of 9 fps, 15 fps and 33, respectively. (c1-c3) represent similar images from 500 $\mu$ m hole and (d1-d3) from 800 $\mu$ m hole. The dotted circle in each image represent the true size of the hole. Mean normalized intensity of the pixels inside the hole at different frame rates from 300 $\mu$ m (b4), 500 $\mu$ m (c4), and 800 $\mu$ m (d4) holes. The error bar indicates the STD of the pixels inside the hole. Table (e) depicts mean  $\pm$  STD of MSRs and CNRs and the averaged NRMSD. The STDs in MSR and CNR were calculated from the 3 repeated measurements on the same hole at the same frame rate. MSRs and CNRs were calculated from the background (red rectangle in (b1)) and the foreground regions (black rectangle in (b1)) from all images..... 46

Figure 4.4. (a) A visual photograph of a dental sample; left and right treatment windows were demineralized for 3 and 7 days, respectively. LIT (b) Amplitude and (c) phase images obtained at 2Hz modulation frequency. (d) segmented demineralized windows. (e) Mean amplitude and STD from the healthy and demineralized areas shown in (d). (f) Mean phase and STD from the healthy and demineralized area shown in (d). (g)  $\mu$ CT slice taken of treatment windows (green arrows). (h) Zoomed area of a treatment window (i) OCT B-scan was taken from the treatment windows along the dashed line in (a). (j) Segmented demineralization areas in blue; average OCT penetration depths: 180  $\mu$ m for 3 days and 163  $\mu$ m for 7 days; average OCT intensities:  $49.52 \pm 27.90$ dB for 3 days and  $54.68 \pm 29.50$ dB for 7 days. .... 49

Figure 4.5(a) Representative LIT amplitude image of LFA spiked with 5ng/ml THC-saliva solution. (b) Two curves obtained at the control and test line by averaging the pixels in the vertical direction of (a). (c) Visual microscopy and LIT comparisons of representative LFAs at different concentrations. (d) Comparison of amplitude metric between panel (c) 6 representative LFAs at concentrations 0, 2, 5, 7.5, 10 and 25 ng/ml. (e) distribution of amplitude metric from all the LFAs at different concentrations (n=240). (f) Comparison of mean amplitude metric among different concentrations. The error bar shows the 99% confidence interval. .... 52

Figure 4.6. (a) Schematic diagram of the lock-in thermography system (b) A use case diagram that depicts a blueprint of the functionalities provided by our developed SDK. (c) A flow chart showing the signal processing method applied to the waveform at each pixel of the image ..... 57

Figure 4.7. Histograms with probability density function (pdf) of the images at the foreground (left) and background region (right) at camera frame rates of 9, 15 and 33 fps for defects at different depths. The panel a, b and c are corresponding to defects 300 $\mu$ m, 500 $\mu$ m and 800 $\mu$ m below intact interrogation surface, respectively. Mean  $\pm$  STD of the pdf are reported in supplementary table 4.1. .... 63

## 1. Introduction

### 1.1. Active Thermography

Active Thermography (AT) refers to a combination of thermographic techniques which are used for non-destructive testing of materials. AT is widely used in different branches of engineering and science, such as for detection of moist areas in the building structures in civil engineering [1], identifying the source of leakage in the electronic components in electrical engineering [2], inspection of the aero-engine parts, space craft components, and primary and secondary structures of airplane in aerospace material [3]. Diagnostic role of temperature in human body has been recognized for centuries [4]. Nowadays in biology and medicine, AT is being used to measure skin thickness, blood flow, skin burns, inflamed regions and detection of early dental caries [5-7].

In AT, sample is excited by an external source and the photothermal responses are registered radiometrically by infrared detectors such as infrared cameras. In presence of internal defects, the temperature field inside the sample gets disturbed and as such leads to a temporal temperature profile different from those captured in intact regions. One of the advantages of AT is the nature of excitation source that can be adapted to the application. Various excitation sources commonly used in AT include optical, mechanical, or electromagnetic [8]. In this thesis, we focus on optical excitation. Based on the temporal pattern of optical excitation used, AT can be further categorized to four categories:

- a. **Pulse Thermography (PT):** PT uses pulses of light to stimulate the sample [9]. As such, PT is based on capturing responses during transient mode of cooling of surface sample. The excitation source is usually lamp, heat gun, etc. PT is particularly used in testing sandwich structures and composites in aircrafts since it can non-destructively inspect large regions of interests in a non-contact and rapid manner [10].
- b. **Lock-In Thermography (LIT):** In LIT, infrared camera captures the thermal wave emitted from the surface in steady-state field (aka thermal-wave field) while sample is being exposed to heat periodically. Radiometrically captured infrared emissions are then processed and converted into signals that are used in calculation of the amplitude and the phase of thermal waves[11, 12]. The phase image in LIT is emissivity-normalized and as such the

effect of non-uniformed heating or variations in sample surface emissivity is not visible in it [13, 14].

- c. **Pulse-Phase Thermography (PPT):** PPT is an innovative method for analysis of the PT data with the phase /frequency concept of LIT [15]. In other words, it is a link between PT and LIT which interrogates at amplitudes and phases of the frequency components excited by pulsed excitation [16].
- d. **Matched-Filter Thermography (MT):** The main limitation in the above mentioned methods is the intrinsic compromise between the inspection depth and the image resolution [17]. That is, to inspect deep in sample lower excitation frequencies are required but this leads to poor resolution, and vice versa. In order to solve this limitation, Matched-filter Thermography (MF) is proposed [17]. In MT, Radar's cross-correlation filtering together with pulse compression techniques such as linear frequency modulation or binary phase coding is used in order to obtain highly resolved images from low-frequency excitations probing deep in the sample [18-20].

In this thesis, we demonstrate the capability of developed low-cost platform in LIT setting.

## 1.2. Lock-in thermography

Among different approaches in active thermography, LIT has proven to offer superior balance between sensitivity to detection of defects and system complexity/cost [21]. In LIT, harmonically intensity-modulated excitation source, such as intensity-modulated lasers, are used to heat up the sample surface which results in creating a modulated temperature field (aka thermal-wave field) inside the sample [22]. Defects inside the sample changes the amplitude and phase of the local thermal wave field by introducing thermal impedances [23] and, as a result, create a detection/diagnostic contrast in the captured infrared emissions from the sample surface. In LIT, the amplitude and phase of infrared emissions from sample surface are accurately calculated using quadrature demodulation (aka lock-in detection).

LIT has been successfully applied in a wide spectrum of industries from interrogation of industrial samples for defects [24] to early diagnosis of diseases in hard and soft tissues [23, 25]. Example applications of LIT in industrial non-destructive testing include determination of fiber orientation in composite [26], measurement of material thermal diffusivity [27], And

detection/visualization of defects such as surface-breaking cracks in samples [28]. In terms of military applications, LIT is increasingly being used in rapid evaluation of defective areas in composite materials used in aerospace structures [29]. One of the first LIT researches for medical diagnosis was the examination of a resin-embedded human tooth[30, 31]. Early diagnosis of dental carries [32] and early stages detection of cutaneous melanoma [25] are other example applications of LIT in medicine.

### 1.3. Theory of Lock-in Thermography

The presence of sub-surface defects acts as thermal impedance to diffusion of heat and as such alter the local amplitude and phase of thermal waves captured by infrared camera from the surface. The infrared emission registered by the infrared camera can mathematically be modeled as a depth integral [23, 33]:

$$s(l, t) \propto \overline{\mu_{IR}} \int_0^l T(z, t) e^{-\overline{\mu_{IR}}z} dz \quad (1.3.1)$$

where  $\overline{\mu_{IR}}$ ,  $l$  and  $T(z, t)$  are the average infrared absorption coefficient of sample in the spectral range of infrared camera, sample thickness/defect depth, and induced thermal wave field in depth  $z$  at time  $t$ , respectively. The ultimate goal of LIT is detection of amplitude and phase of thermal wave field ( $T(z, t)$ ). For example, thermal wave field of a semi-infinite opaque material is expressed as

$$T(z, t) = \frac{Q}{2\sqrt{\rho k c \omega}} e^{\left(\frac{-z}{\mu}\right)} e^{i\left(\omega t - \frac{z}{\mu} - \frac{\pi}{4}\right)} \quad (1.3.2)$$

Where  $Q$ ,  $\mu$ ,  $\rho$ ,  $k$ ,  $c$  and  $\omega$  are the thermal source intensity, thermal diffusion length, sample density, thermal conductivity, specific heat and laser modulation angular frequency, respectively. As shown in this formula, thermal waves exponentially dissipate with depth and the rate of this exponential dissipation is a function of the thermal diffusion length ( $\mu$ ). Thermal diffusion length is defined as the depth at which thermal wave amplitude reduces to  $e^{-1}$  of its initial value and is normally considered as the maximum inspection depth. Thermal diffusion length can mathematically be expressed as:

$$\mu = \sqrt{2\alpha/\omega} \quad (1.3.3)$$

That is, thermal diffusion length is inversely proportional to the modulation frequency ( $\omega$ ) and directly proportional to medium thermal diffusivity ( $\alpha$ ). This means that inspection of the depth of the sample can be controlled by adjusting the modulation frequency. At low frequencies, thermal waves are less dissipated and as such can inspect deep into samples while at high frequencies inspection is superficial. However, by increasing the modulation frequency, and consequently reducing the thermal diffusion length, the spatial resolution of the Lock-in images is increased.

Lock-in demodulation is a signal processing technique for retrieving the amplitude and phase of a signal with known modulation frequency in a noisy channel. In the context of LIT, the intensity of laser excitation is modulated at a particular/known modulation frequency (aka lock-in frequency) based on desired inspection depth and image resolution; therefore, lock-in demodulation is carried out at this known modulation/lock-in frequency. To perform demodulation, camera frame signals ( $ASin(\omega_0t + \varphi)$ ) with unknown amplitude ( $A$ ) and initial phase ( $\varphi$ ) are mixed with in-phase ( $\sin(\omega_0t)$ ) and quadrature ( $\sin(\omega_0t + 90)$ ) reference signals, weighted and low pass filtered to get in-phase ( $S^0$ ) and quadrature ( $S^{90}$ ) images (Figure. 2). Amplitude ( $A$ ) and phase ( $\varphi$ ) of radiometric signals can then be found from the in-phase and quadrature images:

$$\begin{aligned} \begin{matrix} \sin(\omega_0t) \times ASin(\omega_0t + \varphi) \\ \sin(\omega_0t + 90) \times ASin(\omega_0t + \varphi) \end{matrix} &\xrightarrow{\text{Mixing}} \begin{cases} \frac{A}{2} [\cos(\varphi) - \cos(2\omega_0t + \varphi)] \\ \frac{A}{2} [\sin(\varphi) - \cos(2\omega_0t + \varphi + 90)] \end{cases} \xrightarrow{\text{Weighting} \times \sqrt{2}} \\ & \hspace{15em} (1.3.4) \\ \begin{cases} \frac{A}{\sqrt{2}} [\cos(\varphi) - \cos(2\omega_0t + \varphi)] \\ \frac{A}{\sqrt{2}} [\sin(\varphi) - \cos(2\omega_0t + \varphi + 90)] \end{cases} &\xrightarrow{\text{LPF}} \begin{cases} S^0 = \frac{A}{\sqrt{2}} \cos(\varphi) \\ S^{90} = \frac{A}{\sqrt{2}} \sin(\varphi) \end{cases} \rightarrow \begin{cases} A = \sqrt{(S^0)^2 + (S^{90})^2} \\ \varphi = \arctan\left(\frac{S^{90}}{S^0}\right) \end{cases} \end{aligned}$$

Alternatively, the amplitude and phase of thermal waves can be directly calculated by applying fast Fourier transform (FFT) to the time lapse signal from each infrared camera pixel. Fourier transformation of time-lapse signal results in a frequency spectrum showing a dominant peak at the modulation/lock-in frequency [34]. Using the complex number found from FFT at the

modulation frequency, amplitude and phase are then calculated. While amplitude images generally offer better SNR, LIT phase images are inherently emissivity-normalized [19] which means systematic errors caused by variations in emissivity of sample surface do not affect phase results.

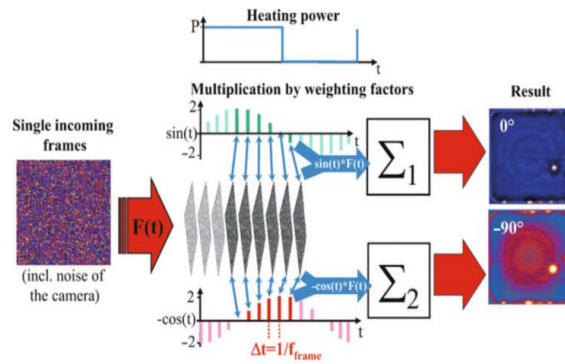


Figure 1.1. The operation of Lock-in [22]

#### 1.4. Objective and outlook of the thesis

Infrared cameras are the key component in LIT. According to black body diagram of the Planck's law at ambient temperature, infrared radiation is maximal at the long wavelength region (LWIR; 8-14 $\mu\text{m}$ ). As such thermal cameras are normally made in the mid-wavelength (MWIR; 3-5  $\mu\text{m}$ ) and LWIR regions. While in the room temperature, the black body diagram peak falls in LWIR which results in considerably higher photon flux to the LWIR sensors [35], the sensitivity of MWIR sensors are superior to those of LWIR sensors. However, the MWIR cameras are usually expensive due to use of bulky external cryogenic cooling system; while, the LWIR cameras with uncooled microbolometer sensors are relatively cheaper [36]. The LWIR camera price is still high ( $\sim$ \$10k-\$100k) when it comes to commercialization of devices for end users. In order to overcome this limitation, we aim to demonstrate feasibility of performing LIT with cell-phone attachment infrared cameras which are both cheaper and smaller in size (almost \$250) when compared to research-grade LWIR infrared cameras [36]. However, incorporating cellphone IR cameras in measurement systems is challenging because:

- a. User is limited to using the manufacturer's application for image acquisition.
- b. User cannot control the cameras attributes (e.g., camera shutter).
- c. Camera frame rates is unstable and low ( $<9\text{fps}$ ).

In this thesis, we offer a system which resolves limitations mentioned above. To this end, we developed a hardware-level code/software for controlling camera attributes in order to achieve stable acquisition of frames at high frame rates. Given the importance of portability we also developed a setting that is both portable and easy to set up. Finally, to demonstrate efficacy of developed system, we performed studies on two high impact areas of detecting early stages of demineralization in human dental enamel and detection and quantification of cannabis in oral fluid. The outcomes of these studies have been disseminated in two journal publications (one published; one in press) as well as one conference proceeding paper. Sections below are brief explanations of the works discussed in these publications as well as my specific contributions to each published work.

#### **1.4.1. Overview of the first paper**

*Thapa D. (co-first author), **Samadi N.** (co-first author), Parkhimchyk, A. and Tabatabaei, N. (2020) Comparison of low cost and research grade active thermography platforms for detection of early dental caries. Proceedings of SPIE, Volume 11354, Optical Sensing and Detection VI; 1135409. <https://doi.org/10.1117/12.2555279>*

The goal of this work was to, qualitatively, compare the performance of the developed low-cost and small size active thermography system to that of our research-grade platform. To do so, we performed imaging on human dental samples with early caries. We chose dental samples for this preliminary study because we have extended experience with these samples using our research-grade active thermography platform [35, 37].

As the first step and in order to overcome the cellphone infrared camera's limitations, we first developed a software development kit (SDK) in C# to enable controlling camera attributes (e.g., shutter control) and acquiring frames at high frame rate via a simple USB interface. Once C# codes were developed, they were included in a Dynamic Link Library (DLL) and called in LabVIEW environment. We then implemented the new SDK in LabVIEW and established the frame acquisition and lock-in program. In the next step, we tested the capability of the new system using artificially-induced early carries in dental samples [23]. Early carries are sub-surface lesions with smaller density compared to the surrounding intact enamel [38]. Existing

clinical methods like X-ray and dental explorers, unfortunately, cannot detect the carries in early stages [39, 40]. Early detection of caries enables remineralization of such lesions and avoids their progression into advanced stages and cavities. Using an artificial demineralization protocol [35, 41], we made treatment windows on two different dental samples and created early caries on healthy human teeth. Samples were then imaged with both high-end and low-cost LIT systems. These preliminary experiments showed the promise of our low-cost platform in producing LIT amplitude and phase images comparable to those obtained from the bulky and expensive research-grade LIT system.

My specific contributions to this work were developing the low-cost LIT system (software and hardware, excluding C# codes), demineralizing the dental samples and conducting the experiments on low cost LIT setup.

Since we managed to establish reasonable performance of our developed low-cost system in this study, in the next steps we carried out more comprehensive studies on the high impact application of detecting THC in oral fluid.

#### **1.4.2. Overview of the second paper**

*Thapa, D. (co-first author), **Samadi, N.** (co-first author), Patel, N., & Tabatabaei, N. (2020).*

*Thermographic detection and quantification of THC in oral fluid at unprecedented low concentrations. *Biomedical Optics Express*, 11(4), 2178-2190.*

<https://doi.org/10.1364/BOE.388990>

Following the legalization of marijuana in Canada and other jurisdictions around the world in recent years, the number of cannabis users is expected to increase. This indicates that there is an urgent need for rapid, yet sensitive, roadside screening devices for testing drivers under the influence of cannabis. Lateral flow immunoassays (LFAs), which are most commonly known for pregnancy tests, are also used in the drug of abuse screening. However, their detection threshold for THC (a principal psychoactive constituent of cannabis) in oral fluid is normally limited to greater than 25 ng/ml which is well above the *per se* limits set by many countries (usually 1 to 5 ng/ml) in order to define impairment, especially with respect to operating motor vehicles.

In the second paper we setup a study in order to test and quantify THC level in oral fluid. To get a better understanding of the technical challenges involved, we used high-end infrared camera in this study. After statistical analysis, results showed LIT system can detect and quantify THC in oral fluid with 98% accuracy. We also performed a visual interpretation human study for comparing the LIT system readings of LFAs to the LFA common interpretation method based on human vision and concluded that accuracy of LIT system was significantly higher than that of LFA visual test. We used the results of this research as a benchmark to validate those of the new low-cost LIT system published in the third paper.

In this paper, my specific contributions were designing, conducting and running visual interpretation test and designing protocols for image processing method for quantifying the THC in LFAs.

Given the promising results of lock-in method on detecting and quantifying of THC in oral fluid, as a next step, we performed a similar study with our low cost LIT system setup.

### **1.4.3. Overview of the final paper**

***Nakisa Samadi** (co-first author), Damber Thapa (co-first author), Mohammadhossein Salimi, Artur Parkhimchyk, and Nima Tabatabaei (2020). Low-Cost Active Thermography using Cellphone Infrared Cameras: from Early Detection of Dental Caries to Quantification of THC in Oral Fluid, *Scientific Reports* 10, Article number: 7857.*

<https://doi.org/10.1038/s41598-020-64796-6>

In this paper, we reviewed the low-cost system setup in further details, elaborating on the key benefits of running the low-cost cameras with our developed software. We then discussed different attributes of cellphone attachment infrared cameras and compared the developed SDK with manufacturer's app. Results showed that our SDK and LabVIEW software significantly outperformed manufacturer's app. We also conducted LIT experiments on a pin-fin thermal heat sink to demonstrate that performing LIT at high frame rate, only offered by our software, leads to better resolution of superficial defects. As a conventional method to check feasibility of LIT systems, we used aluminum blocks with the different blind holes of different depth and showed that our system could differentiate holes with different depths. We then examined performance

of our system on two high impact applications that are early detection of dental carries and detection of THC in oral fluid.

Dental carries are the main cause of the tooth lost in all ages, they are considered as one of the major public health challenge[42]. Early detection of dental carries is important since they are preventable if they are detected in early stages. In the first manuscript we demonstrated that detection performance of developed low-cost system is reasonably comparable to that of the expensive research-grade system. Given this conclusion, in the third manuscript, we performed a more detailed and quantitative study on detection of early dental caries and compared the performance of our low-cost system to x-ray and optical coherence tomography (OCT) as a standard-of-care and an emerging caries detection technology in the field, respectively. The analytical calculations showed that the developed low-cost system can successfully detect the carries as well as distinguished them from each other base on the stage of decay, outperforming both x-ray and OCT.

In our second paper, we successfully quantified THC in oral fluid using LIT method. Using a research grade camera is expensive and not feasible for performing driver testing onsite. To that end, we evaluated the performance of our low-cost system which is both portable and inexpensive. In performing these experiments, we used LFAs which were made for the second paper. In the third paper, we followed similar procedures for image processing to those used in the second paper and showed that our low-cost system can also detect and quantify THC amount in oral fluid at an unprecedented low detection threshold of 2ng/ml; a task not achievable by any commercially available point-of-need devices in the market. Our demonstration on the possibility of measuring THC in oral fluid with the low-cost system, enables commercialization of a point-of-need portable device, for roadside or workplace, for detecting and quantifying THC.

My contributions to the third paper were designing and developing the low-cost LIT system (software and hardware), performing LIT experiments, analyzing the data/images and collaborating in the statistical analysis of data.

The remainder of this thesis is organized as follows. Chapter one, two, and three include the published manuscript of papers in the sequence explained above. Finally, we review concluding remarks and explain future research avenues.

# CHAPTER TWO

## Comparison of low cost and research grade active thermography platforms for detection of early dental caries

D. Thapa<sup>a +</sup>, N. Samadi<sup>a +</sup>, A. Parkhimchyk<sup>a</sup>, and N. Tabatabaei<sup>a</sup>

<sup>a</sup>Department of Mechanical Engineering, Lassonde School of Engineering, York University

<sup>+</sup>these authors contributed equally to this work

*Note: This chapter is a modified version of the published paper*

### 2.1. Abstract

Active Thermography (AT) has been actively explored in recent years for the early detection of demineralization in dental enamel. AT utilizes a highly expensive thermal camera; the price of research-grade thermal cameras ranges between \$10k-\$200k. In an attempt to reduce the cost and size of the AT, we recently demonstrated the possibility of incorporating low-cost (~\$250) cell-phone attachment long-wave infrared cameras for lock-in thermography (LIT). In this work, we validate our developed low-cost LIT system by comparing its measurement with those of the high-end research grade LIT system consisting of an expensive research-grade camera for detecting early dental caries. Artificially-induced caries are created on healthy enamel surfaces of extracted human teeth and imaged by both low-cost and high-end LIT systems. Comparative measurements reveal that the caries locations and sizes captured by the low-cost system are consistent with those of the high-end system. This low-cost LIT imager promises an affordable solution for the examination of teeth, which can benefit patients in rural and underdeveloped areas to reduce health care disparities.

### 2.2. Introduction

Dental caries is one of the most prevalent chronic diseases among all ages, affecting around 2.4 billion people worldwide [1]. Caries are bacterial infections that causes localized destruction of

the tissues of the tooth [2]. Early caries is sub-surface lesion and is slightly softer than the adjacent sound enamel surface [3]. The initial carious lesion that is detectable clinically is called “white spot lesions” [2]. The most common techniques for detecting caries are the visual-tactile and dental radiographs. However, these methods are not sensitive enough for detecting early or hidden forms of dental caries [4]. Radiographic imaging cannot detect small lesions on the order of 50-500  $\mu\text{m}$  in the interproximal areas, therefore, they have minimal diagnostic value for early caries detection [5-6]. Studies have also suggested that both dental x-rays [7-9] and dental explorers (tools used for visual-tactile) [10-11] are inefficient for the diagnosis of occlusal surface caries. Early caries can be remineralized if detected early and appropriate preventive measures introduced [12]. To practice minimal intervention dentistry or attempts to remineralize, arrest or harden carious lesions in their early stages, there is a clear need for more sensitive detection methods.

In recent years, various optics-based techniques have been explored to address the need for early detection of dental caries so that a proper preventive and remineralization approach can be utilized to halt the progress of the disease process. Among the numerous methods, photothermal radiometric methods, such as active thermography (AT) methods have been actively explored in recent years for the early detection of demineralization in dental enamel [13-19]. AT was used for the first time by Tabatabaei et al. [14] for imaging simulated early caries in extracted human teeth and demonstrated that AT exhibits superior sensitivity to very early stages of demineralization compared to polarized Raman spectroscopy [15]. A more recent study by Shokouhi et al. [18] shows that AT provides better sensitivity and detection threshold in detecting very early stages of simulated caries in extracted human teeth compared to cross-polarization spectral-domain optical coherence tomography (OCT). They were capable of detecting artificially induced caries at early as 2 days of demineralization window using lock-in thermography (LIT) which was not detected by visual inspection as well as by a high-resolution OCT. In addition, the detection specificity of LIT was significantly better than that of OCT which considerably reduces the false positive readings and allows for proper identification of early carious regions from the sound enamel region [18]. These aforementioned findings show that AT promises to be a noninvasive method for arresting carious lesions in their early stages and has the potential for translation into clinical applications. Despite these promising results, AT utilizes an expensive thermal camera; the price of research-grade thermal cameras, ranges

between \$10k-\$200k, posing a key barrier to the wide adoption of this technology. To overcome these shortcomings, we have recently developed a low-cost LIT system by incorporating a cell-phone attachment camera (~\$250) instead of the costly research-grade infrared cameras and demonstrated the possibility of imaging artificially induced early dental caries [16-17]. Although promising, the results of cellphone attachment camera for detecting dental caries were not validated by comparing its results with a high-end LIT system. In this work, we aim to validate the performance of the low-cost LIT system for detecting early stages of demineralization in human dental enamel, by comparing its measurements with the corresponding measurements obtained from a high-end LIT system consisting of an expensive research-grade camera.

## **2.3. Methods**

### **2.3.1. Dental sample preparation**

The anonymous human teeth collected from local oral surgeons were stored in distilled water inside the fume hood to prevent dehydration. In order to induce caries in the tooth in a controlled manner, an acidified gel [18] that mimic the properties of bacterial plaques on enamel was used. Two teeth with no visual defect were selected for this experiment and named s1 and s2 for the sake of simplicity. The selected tooth was rinsed thoroughly with distilled water and dried in the air before exposure to the demineralizing gel. To achieve localized demineralization, the surface of the tooth was shielded by transparent nail polish, leaving a small window (aka treatment window) exposed. The samples were then submerged upside down in a test tube containing 25 ml of acidified gel for 5 days. The samples were then removed from the test tube, rinsed under running water, removed nail polish using Acetone and rinsed again with distilled water.

### **2.3.2. Lock-in-Thermography: principles and instrumentations**

The principle of LIT is based on the introduction of the intensity-modulated light source to produce a thermal contrast between the defected areas (lesions) and the healthy area of the sample [20]. The induced local surface temperature modulation is subsequently captured by an infrared camera which after signal processing yields an amplitude and a phase image. In this configuration, the presence of defects/inhomogeneity (e.g. carious lesions), alters the surface temperature profiles registered by the camera, which produces a contrast difference between the

intact and defective regions in the amplitude and phase images. The presence of lesions, normally, increases the amplitude values that characterized the reduction in thermal conductivity of the sample due to the damage in the tissue. The lesions also alter the center of gravity of the thermal-wave field due to the thermal impedance, that results in contrast difference between the lesions and sound enamel regions in the phase image.

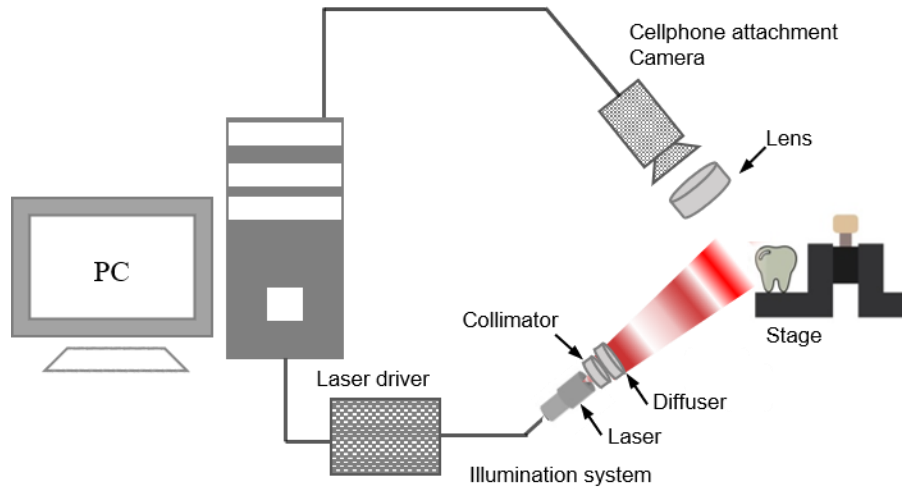


Figure 2.1. (a) Schematic illustration of the experimental set-up of a cellphone-based Lock-in-Thermography

Figure 2-1 depicts the experimental setup of our low-cost LIT system. Light from the excitation source (Continuous-wave near-infrared laser  $\lambda=808\text{nm}$ ; Jenoptik, Jena, Germany) is collimated (Thorlabs, Newton, New Jersey, USA, F220SMA-780), homogenized (Thorlabs, Newton, New Jersey, USA, ED1-C20-MD), intensity-modulated (National Instruments, Austin, Texas, NI USB-6363 BNC) and impinged onto the sample. The detection subsystem includes a low-cost cellphone attachment infrared camera (Seek thermal compact; Seek Thermal Inc.; Android) in conjunction with a CO<sub>2</sub> laser cut Zinc Selenide objective lens ( $f = 1''$ ). The area imaged by the camera ( $156 \times 207$  pixels) is  $7.43 \times 9.86 \text{ mm}^2$  that corresponds to the spatial pixel size of  $\sim 48 \times 48 \mu\text{m}^2$ . While the nominal frame rate of the camera through its standard applet is less than 9fps, we have deciphered the communication protocol and frame information structure of the camera and managed to utilize USB 2.0 documentation and Microsoft Windows native application programming interfaces (APIs such as WinUSB and SetupAPI) to set up packets of information

and send them to the cameras' default endpoint address and, subsequently, acquire frame data from the camera through a corresponding pipe. As such, the developed platform not only enables control of camera attributes but also offers reliable acquisition of frames at constant frame rates of up to 33 fps through a simple USB interface [17].

After acquiring frames from the low-cost system, the effect of bulk heating is removed from the temporal signal by fitting a polynomial curve. After testing curves of different orders, we discovered a polynomial curve of order seven to be the optimum compromise between efficiency and required computation power. Then, a fast Fourier transform (FFT) is applied to the waveform, followed by determination of the magnitude and phase of the complex number corresponding to the laser modulation frequency in the Fourier domain. A detailed explanation of lock-in-demodulation that describes the process of obtaining an amplitude and phase images from the camera row frames can be found in our previous papers [16-17].

The experimental setup of the high-end LIT system is basically the same as described in our previous paper [21-22] that consisted of a long-wave infrared camera (Xenics Gobi 640, Belgium, spectral range 8-14 $\mu$ m) and captures raw camera frames at 100 frames per second. The area imaged by the camera (240  $\times$  320 pixels) is 9.84 $\times$ 13.11 mm<sup>2</sup> that corresponds to the spatial pixel size of  $\sim$ 41 $\mu$ m. To take LIT images, the sample was securely mounted on a LEGO block and subsequently imaged by both systems at a laser modulation frequency of 1Hz.

## **2.4. Results and Discussion**

Figure 2.2 a-b show the amplitude image and phase image, respectively of sample s1 from the low-cost LIT system. The presence of lesion due to the effect of demineralization is clearly visible in both amplitude (Figure 2.2 a) and phase (Figure 2.2 b) images. The corresponding images from the high-end LIT system are shown in Figure 2.2 c-d. The presence of a lesion, its shape, and size detected by the low-cost LIT system are comparable to those obtained from the high-end LIT system, Figure 2.2 c-d. Transfer function was applied on all images in order to remove systemic inhomogeneities. To do so, a semi-infinite Aluminum block sample with uniform surface condition was imaged with identical experimental conditions to those used in dental caries studies. Then, amplitude and phase compensation factors for each pixel (aka

transfer function) was calculated for removal of any inhomogeneities caused by illumination and optical zoom sub-systems. Although we intended to demineralize a rectangular area of the tooth sample, the effect of the acidic gel is not homogeneous within the treated window, causing some areas more demineralized than others. The low-cost LIT system is capable of detecting carious locations as correctly as the high-end LIT system as the features of the lesions obtained from these imaging systems are almost identical which confirms that the low-cost system is highly sensitive to differentiate the different stages of demineralization. The amplitude image, Figure 2.2 (a), shows a higher amplitude values in the demineralized area compared to the surrounding intact areas, this is due to the enhanced local absorption of laser light in the carious region by demineralization by-products. This indicates that the thermal conductivity is reduced in the demineralized regions due to the damage in the tissue. The phase image, Figure 2.2 (b), also show a different contrast in the demineralized area compared to the healthy intact areas, this is because the enhancement of light absorption in caries region shifts the local centroid of the thermal wave field, causing a phase shift in the thermal signals compared to those of the surrounding intact areas. The amplitude images of both systems offer better signal-to-noise ratio (SNR) between the carious region and the healthy intact regions; however, phase images are inherently emissivity-normalized and as such not prone to errors caused by variations in emissivity of the sample surface, therefore, the phase image information is complementary to those of the amplitude image. The phase images are capable to depict signals from natural caries as shown by the arrow in Figure 2.2 (b) and (d) which was not visible by the visual inspection.

The low-cost LIT amplitude and phase images of sample s2 are shown in Figure 2.3 a-b, respectively. Similarly, the corresponding images from the high-end system are shown in Figure 2.3 c-d. Similar to sample s1, the amplitude and phase images of sample s2 obtained from the low-cost system are consistent with those of the high-end LIT system. Both systems have shown increased contrast in the amplitude and phase images at caries sites compared to the healthy intact areas.

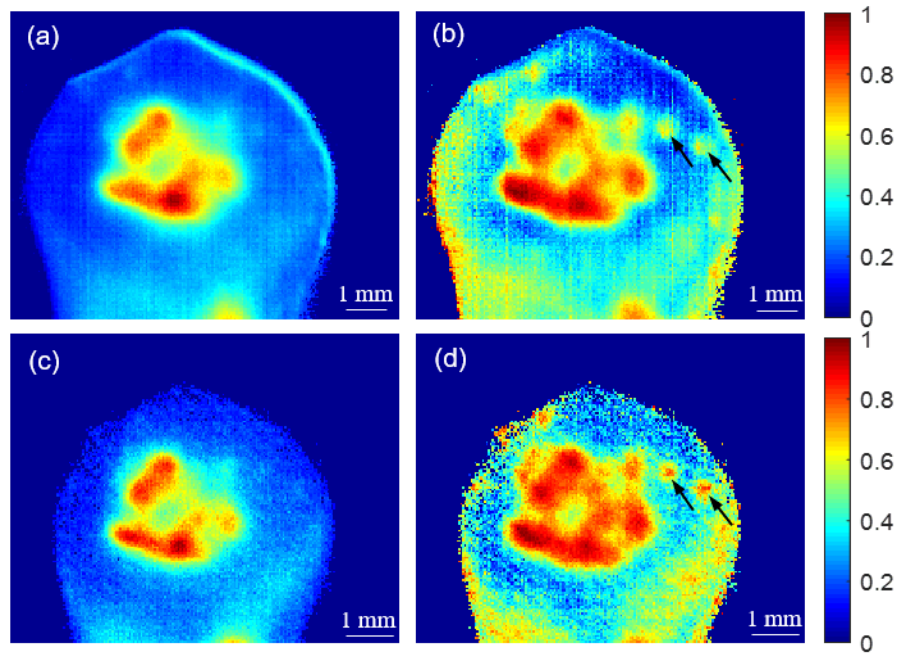


Figure 2.2. : LIT amplitude (a) and phase (b) images of a dental sample s1 taken by the low-cost LIT system. The corresponding amplitude (c) and phase image (d) from the high-end research grade LIT system

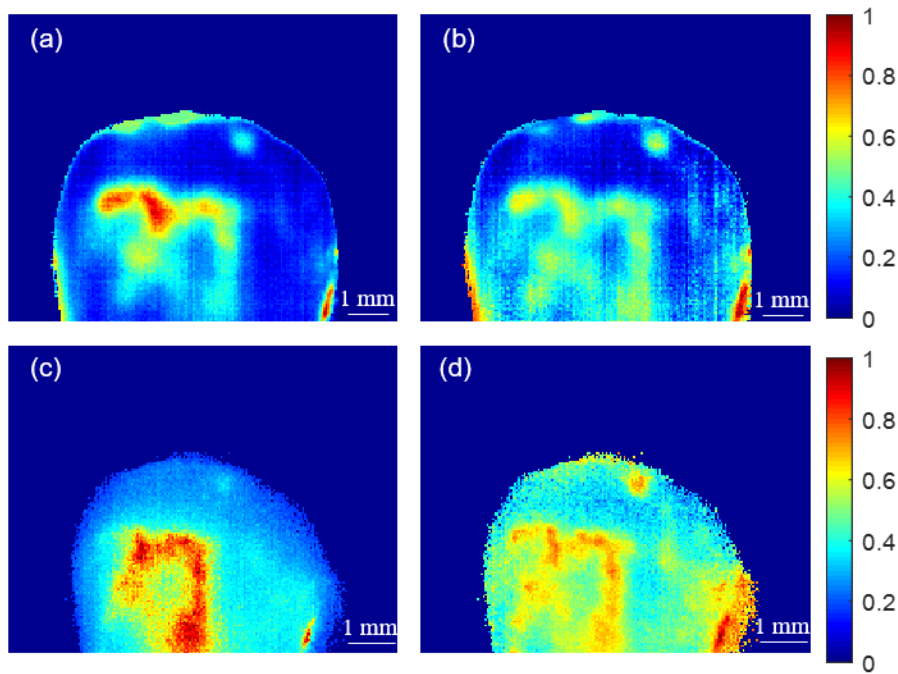


Figure 2.3. LIT amplitude (a) and phase (b) images of a dental sample s2 taken by the low-cost LIT system. The corresponding amplitude (c) and phase image (d) from the high-end research grade LIT system

## 2.5. Conclusion

In this study, we validate our developed low-cost LIT system for detecting early caries in extracted human teeth by comparing its measurement with those of the high-end LIT system consisting of an expensive research-grade camera. The results show that the developed low-cost system is capable of detecting artificially-induced caries created on healthy enamel surfaces as good as those perceived by the high-end LIT system. Comparative measurements of dental caries revealed that the enhancement in contrast in the amplitude and phase images at caries sites due to demineralization by-product is clearly visible in the images captured by the low-cost system. This low-cost system can be used for the detection of the early carious lesion if translated into the clinical settings. One of the key advantages of the LIT system is that the inspection depth can be controlled via the intensity-modulation frequency of external excitation source. As a result, sub-surface defects, such as caries, can be detected by reducing the modulation frequency, while superficial defects such as erosions can be captured by using high modulation frequencies.

The results reported in this manuscript are from the benchtop prototype system. We are currently pursuing the development of a dental handheld imager using the low-cost cellphone attachment camera. We plan to perform ex-vivo validation studies with this handheld device on dental matrices and possibly artificial mouth system. We anticipate that further development of this low-cost LIT system can significantly lower the cost of LIT and hence paving the way for the translation of AT techniques to the clinical applications. The low-cost examination of teeth can benefit patients in rural areas and underdeveloped countries to reduce health care disparities.

## 2.6. References

- [1] Kassebaum, N. J., Bernabé, E., Dahiya, M., Bhandari, B., Murray, C. J. L., & Marcenes, W. "Global burden of untreated caries: a systematic review and metaregression." *J. Dent. Res.* 94(5), 650-658 (2015).
- [2] Samaranayake, L. [Essential microbiology for Dental students], pp.267, (2006).
- [3] Roopa, K. B., Pathak, S., Poornima, P., & Neena, I. E. "White spot lesions: A literature review," *J. Pediatr Dent.* 3(1), 1 (2015).
- [4] National Institutes of Health Consensus Development Conference Statement. "Diagnosis and Management of Dental Caries throughout Life," *J. Dent. Educ.* 65(10), 1162-8 (2001).
- [5] McKnight-Hanes, C., Myers, D. R., Dushku, J. C., Thompson, W. O., & Durham, L. C. "Radiographic recommendations for the primary dentition: comparison of general dentists and pediatric dentists," *Pediatr Dent.* 12(4), 212-216 (1990).

- [6] Flaitz, C. M., Hicks, M. J., & Silverston, L. M. "Radiographic, histologic, and electronic comparison of basic mode videoprints with bitewing radiography," *Caries Res*, 27(1), 65-70 (1993).
- [7] Hintze, H., & Wenzel, A. "Clinically undetected dental caries assessed by bitewing screening in children with little caries experience.," *Dentomaxillofac. Radiol.*, 23(1), 19-23 (1994).
- [8] Nyttun, R. B., Raadal, M., & Espelid, I. "Diagnosis of dentin involvement in occlusal caries based on visual and radiographic examination of the teeth," *Eur. J. Oral. Sci*, 100(3), 144-148 (1992).
- [9] Flaitz, C. M., Hicks, M. J., Silverstone, L. M. "Radiographs, histologic and electronic comparison of occlusal caries: An in vitro study," *Paediatr Dent*, 8(1): 24-28 (1986).
- [10] Penning, C., Van Amerongen, J. P., Seef, R. E., & Ten Cate, J. M. "Validity of probing for fissure caries diagnosis," *Caries Res*. 26(6), 445-449 (1992).
- [11] Lussi, A. "Comparison of different methods for the diagnosis of fissure caries without cavitation," *Caries Res*. 27(5), 409-416 (1993).
- [12] Backer, D. O. "Post-eruptive changes in dental enamel," *J Dent Res*, 45: 503-551 (1966).
- [13] Ojaghi, A., Parkhimchyk, A., & Tabatabaei, N., "First step toward translation of thermophotonic lock-in imaging to dentistry as an early caries detection technology," *J. Biomed. Opt.* 21, 096003 (2016).
- [14] Tabatabaei, N., Mandelis, A., & Amaechi, B. T. "Thermophotonic lock-in imaging of early demineralized and carious lesions in human teeth," *J. Biomed. Opt.* 16, 071402 (2011).
- [15] Tabatabaei, N., Mandelis, A., Dehghany, M., Michaelian, K. H., & Amaechi, B. T. "On the sensitivity of thermophotonic lock-in imaging and polarized Raman spectroscopy to early dental caries diagnosis," *SPIE* (2012).
- [16] Razani, M. Parkhimchyk, A., & Tabatabaei, N. "Lock-in thermography using a cellphone attachment infrared camera," *AIP Adv.* 8, 035305 (2018).
- [17] Samadi, N., Thapa, D., Salimi, M., Parkhimchyk, A., and Tabatabaei, N., "Low-cost active thermography using cellphone infrared cameras: from early detection of dental caries to quantification of THC in oral fluid," *Sci. Rep.* (2020), In Press.
- [18] Shokouhi, E. B., Razani, M., Gupta, A., & Tabatabaei, N. "Comparative study on the detection of early dental caries using thermo-photonic lock-in imaging and optical coherence tomography, *Biomed.*" *Opt. Express.* 9, 3983-97 (2018).
- [19] Ojaghi, A., Parkhimchyk, A., & Tabatabaei, N. "Long-wave infrared thermophotonic imaging of demineralization in dental Hard tissue," *Int. J. Thermophys.* 37(2016).
- [20] G. M. C. T. Astarita, [Infrared Thermography for Thermo-Fluid-Dynamics] 1st ed. (Springer-Verlag Berlin Heidelberg, 2013).
- [21] Thapa, D., Samadi, N., Patel, N., & Tabatabaei, N. "Thermographic detection and quantification of THC in oral fluid at unprecedented low concentrations," *Biomed. Opt. Express*, 11(4), 2178-2190 (2020).
- [22] Thapa, D., Samadi, N., Patel, N., & Tabatabaei, N. "Enhancement of sensitivity and detection limit of lateral flow immunoassay using lock-in thermography," *Proc. SPIE*, 11361, Biophotonics in Point-of-Care, 113610M (2020).

## CHAPTER THREE

### Thermographic Detection and Quantification of THC in Oral Fluid at Unprecedented Low Concentrations

Damber Thapa,<sup>†</sup> Nakisa Samadi,<sup>†</sup> Nisarg Patel, and Nima Tabatabaei\*  
Department of Mechanical Engineering, Lassonde School of Engineering, York University  
<sup>†</sup>Equal contribution

*Note: This chapter is a modified version of the published paper*

#### 3.1. Abstract

With recent changes in the legalization of cannabis around the world, there is an urgent need for rapid, yet sensitive, screening devices for testing drivers and employees under the influence of cannabis at roadside and workplace, respectively. Oral fluid lateral flow immunoassays (LFAs) have recently been explored for such applications. While LFAs offer on-site, low-cost and rapid detection of tetrahydrocannabinol (THC), their nominal detection threshold is about 25 ng/ml which is well above the 1-5 ng/ml *per se* limits set by regulations. In this paper, we report on the development of a thermo-photonic imaging system which utilizes the commercially available low-cost LFAs but offers detection of THC at unprecedented low concentrations. Our reader technology examines photothermal responses of gold nanoparticles (GNPs) in LFA through Lock-In Thermography (LIT). Our results (n=300) suggest that the demodulation of localized surface plasmon resonance responses of GNPs captured by infrared cameras allows for detection of THC concentrations as low as 2 ng/ml with 96% accuracy. Quantification of THC concentration is also achievable with our technology through calibration.

#### 3.2. Introduction

Cannabis and its byproducts are the most widely used psychoactive substances worldwide [1]. According to the World Health Organization, about 147 million people, 2.5% of the world

population, consume cannabis [2], and yet this number is expected to increase in the wake of the recent legalization of Cannabis in Europe and North America [3]. While cannabis affects people differently, most studies suggest that consuming cannabis impairs coordination, memory, associative learning, attention, cognitive flexibility, and, to a certain degree, the reaction time of users [4]. More importantly, cannabis impairment is found to be highly correlated with driving skills; the higher the impairment, the worse the driving-related skills [5]. Accordingly, the risk of fatal accidents is significantly increased while driving under the influence of cannabis [6-7] and since young adults are the most frequent users of cannabis in Europe and North America [8-9], cannabis is believed to be an important contributor to the elevated risk of motor vehicle accidents in younger populations [10-13].

With widespread worldwide trends in the legalization of cannabis, driving a motor vehicle while impaired has become a pressing matter for governments. Many jurisdictions in Europe and North America have recognized the urgent need to regulate the impairment aspects of the legalization of cannabis and formalized that operating a motor vehicle while impaired is prohibited. However, since the determination of impairment is not a straightforward matter, regulating bodies has established *per se* limits for the concentration of Tetrahydrocannabinol (THC; a principal psychoactive element of cannabis) as a key measure in determining impairment. Existing *per se* limits for THC are defined in the whole blood/plasma and vary widely between jurisdictions (1 to 5 ng/ml). Nonetheless, accurate measurement of THC in blood has proven to be challenging as withdrawal of blood samples need to take place in medical facilities, causing a significant delay in sampling (usually 1-2 hours) during which THC concentration in the blood dramatically drops [14]. To overcome this systematic source of error in screening, and allow for proper enforcement of regulations, law enforcement in most jurisdictions have advocated and, even regulated, the use of devices that screen and measure THC in accessible bodily fluids such as oral fluid [15]. Screening THC in oral fluid allows for easy collection of samples in public and provides rapid analysis without the need for sophisticated equipment and highly trained/medical personnel. Studies suggest a close correlation between the concentration of THC in blood and oral fluid, especially about half an hour after consumption [16].

Reliable screening and measurement of THC in the workplace is another pressing need in the wake of the legalization of cannabis; especially since cannabis is the most commonly found drug among workers in many countries [17-21]. While the burden of proof for detecting THC in the

workplace is, normally, lower than that of roadside, workplace safety is by far a larger need, encompassing the majority of the 3.1 billion USD global market of drug of abuse testing. Workplace safety field studies suggest that acute intoxication from cannabis smoking significantly impair employees' performance, leading to increased risks of work-related accidents [22]. Traditionally, urinalysis testing has been the choice for testing drugs in the workplace. However, studies suggest that urine tests have poor validity and low sensitivity to detect employees who represent a safety risk mostly because (1) THC has a long half-life of elimination in urine and can be detected in urine up to weeks after last use among heavy users, obcluding the correlation between urinalysis positive test and impairment at time of sample collection. (2) the privacy considerations in collecting urine samples allow for tampering with sample collection, jeopardizing the validity of urine test results.

Irrespective of market (workplace vs roadside), laboratory-based analytical techniques based on chromatographic separation procedures, such as gas chromatography-mass spectrometry (GC-MS) [23], gas chromatography-tandem mass spectroscopy (GC-MS/MS) [24], liquid chromatography-tandem mass spectrometry (LC-MS/MS) [25], high-performance liquid chromatography (HPLC) [26], are considered as the gold standard for detecting and quantifying THC. While these laboratory-based methods are highly sensitive and specific for cannabinoid detection, they are expensive, complex and laborious because they not only involve lengthy sample preparation and chromatographic separation procedures but also are, normally, carried out by highly trained personnel in a controlled laboratory environment. Long turnaround time is another limitation of laboratory-based analytical methods because in most scenarios impaired person needs to be immediately identified and isolated in order to prevent immediate acute events. To overcome the challenges of THC screening in blood and urine, technologies testing oral fluids using affinity chromatography methods, such as lateral flow immunoassays (LFAs), have recently been explored both at the workplace and roadside [27-28]. Oral fluid LFA technologies offer simple, low-cost, portable, and rapid detection of THC. However, the detection threshold of THC in commercially available LFAs is normally limited to greater than 25 ng/ml, which is insufficient for proper enforcement of workplace and roadside *per se* regulations.

In this manuscript, we demonstrate how thermographic interrogation of commercially-available low-cost oral fluid LFAs with a nominal detection limit of 25ng/ml can offer an order of

magnitude improvement in detection limit, enabling reliable detection and quantification of THC at concentrations as low as 2ng/ml. Interpretation of LFAs is, normally, carried out either visually or using a reader based on the intensity of visible-light scattering from immobilized gold nanoparticles (GNPs). Our innovation [29], on the other hand, explores the light absorption thermal signatures of GNPs in response to modulated laser illumination [30] in order to minimize background noise levels and improve detection performance. Our results (n=300) suggest that the demodulation of thermal-wave responses of GNPs through lock-in demodulation of radiometric signals registered by infrared cameras (aka. Lock-In Thermography; LIT) allows for detection of THC concentrations as low as 2 ng/ml with an accuracy of 96%. Another key differentiator of our technology is its ability to reliably quantify THC concentration using commercially available and low-cost LFAs through calibration. In this manuscript, we also offer and discuss the statistical comparison of the detection performance of developed technology against those of human visual interpretation.

### **3.3. Methods**

#### **3.3.1. Lateral flow immunoassay**

Lateral flow immunoassays are simple paper-based devices used for point-of-care diagnostics in a broad spectrum of fields, spanning from agriculture to medicine to food and environmental testing. A typical LFA strip consists of four major components; sample pad, conjugate release pad, detection zone, and absorbent pad, all mounted on a plastic backing card as shown schematically in Figure 3.1.

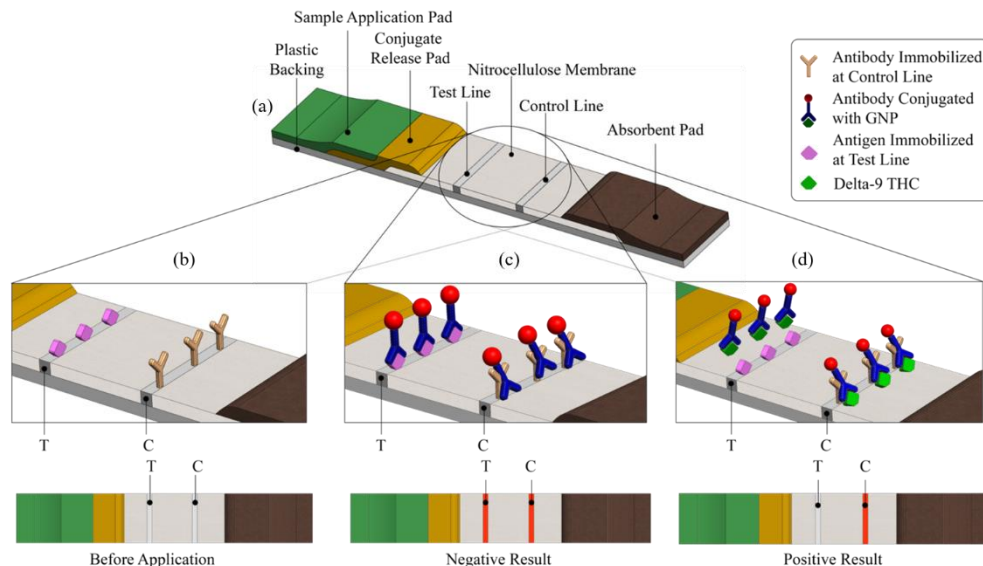


Figure 3.1. (a) Schematic diagram of LFA test strip. Schematic illustration of binding mechanisms of competitive LFAs (b) before use, (c) negative test, and (d) positive test with their respective visual appearance.

For detection of small size analytes such as THC, a competitive LFA format, in which an increase in analyte concentration yields reduction of color intensity in test band, is often used. In such design, the sample (e.g., oral fluid) applied at the sample pad migrates into the conjugate release pad that contains the primary antibody conjugated to the colored particles (usually GNPs). An antibody is a special type of protein responsible for binding to specific antigens or other molecules during immunoassay. Based on their binding capability, they are broadly divided into primary and secondary antibodies. Primary antibodies are those antibodies that bind to other antibodies, antigen or any other substance of interest, whereas secondary antibodies are those antibodies that bind to primary antibodies. Antigens are typically proteins peptides, or polysaccharides, responsible for binding to antibodies to form an antigen-antibody complex. Therefore, during the immunoassay, the primary antibody-GNP conjugates attach to analyte in the conjugate release pad and flow along the strip to enter the detection zone. The detection zone consists of antigen immobilized at the test band and secondary antibody immobilized at the control band. The antigen has the ability to bind with the primary antibody while the secondary antibody has the ability to bind with labeled antibody conjugate. Small analytes, such as THC have a single antigenic determinant and hence cannot bind to two antibodies simultaneously. Therefore, if the analyte is present in the sample it binds with the primary antibody and hence blocks the binding between the antigen and primary antibody, resulting in absence of color in the

test line. On the other hand, if the target analyte is absent, the primary antibody binds to the antigen immobilized in the test band and a strong color line is seen in the test line (negative test). The presence of the control line ensures that the test is performed correctly. In Figure 3.1b and in Figure 3.1c, schematically, show binding mechanism and visual presentation of positive and negative tests in competitive LFA design. The absorbent pad absorbs the excess sample and prevents the backflow of the liquid [31]. In this study, commercially available oral fluid LFA strips for detection of THC (NarcoCheck™ saliva test strips, Kappa city Biotech SAS, Montluçon, France) with a nominal detection limit of 25ng/ml were used.

### **3.3.2. Preparation of oral fluid-THC solutions and LFA test strips**

To examine the response of our technology to different concentrations of THC in oral fluid, the standardized recipe of the Canadian Society of Forensic Science Drugs and Driving Committee was followed [32]. That is, a known volume of Delta-9 THC stock solution (MilliporeSigma; Oakville, Canada) was mixed with non-stabilized artificial saliva (Pickering Laboratories, Inc, Mountain View, California, USA) to attain the desired THC concentrations of 25, 10, 7.5, 5, 2 and 0 ng/ml. To study the reproducibility, ten (10) LFAs were spiked with 150ml of solution at each THC concentration. The LFA strips were then interpreted by visual and LIT methods.

### **3.3.3. Lock-In Thermography Interpretation of LFAs**

A schematic of the custom-made lock-in thermography system used in this study is depicted in Figure 3.2(a). While detailed information about the system can be found elsewhere [33-36], in short, an intensity-modulated near-infrared light (808nm Multimode Pumping Fiber Coupled Laser Diode, Hangzhou Brandnew Technology Co., Ltd, Hangzhou, China) was collimated (F220SMA-780 collimator, Thorlabs Inc, Newton, USA), homogenized (ED1-C20-MD diffuser, Thorlabs Inc, Newton, USA), and impinged onto the sample (Figure 3.2.a). A multifunctional data acquisition unit (National Instruments, Austin, Texas, NI USB-6001) was used to modulate the laser intensity at the desired modulation frequency. Here, we used 1Hz laser modulation frequency to illuminate the sample. The average optical intensity on the sample surface was 2.7 W/cm<sup>2</sup>. Radiometric detection was synchronously carried out via a long-wave infrared camera (Xenics Gobi 640, Belgium, wavelength range 8-14µm) at 100 frames per second through a frame grabber (Euresys, Angleur, Belgium, Grablink Full) and via Cameralink interface. A 24

mm focal-length objective lens was used to focus the camera on the surface of the LFAs. Lock-in demodulation of acquired thermal camera signals was performed in the LabVIEW environment to obtain the amplitude of ensuing thermal waves at each pixel [33-36].

MATLAB software (MathWorks, Version R2017a) was used for analyzing the amplitude images. A representative amplitude image is shown in Figure 3.2b. The analysis software calculates the average intensity of pixels over all the columns in a strip, as shown in Figure 3.2c. To minimize the systematic errors induced by day-to-day variations in laser illumination system and manufacturing of LFAs, the contrast of LFA test strips in amplitude image were normalized by scaling the image contrast between those of the surrounding white nitrocellulose paper (red rectangle in Figure 3.2b) and control line. After normalization, the average intensity of pixels over all the columns in a strip was calculated, which generated two bell-shaped curves at the control and test bands, as shown in Fig 2c. For quantitative analysis, a metric was defined as the average of the amplitude values within the full width at half maximum (FWHM) of the test line curve (between points A and B in Figure 3.2c). Throughout this manuscript, we will adopt this metric as a normalized amplitude value and use it for calibration and quantitative comparison of LFAs at different concentrations.

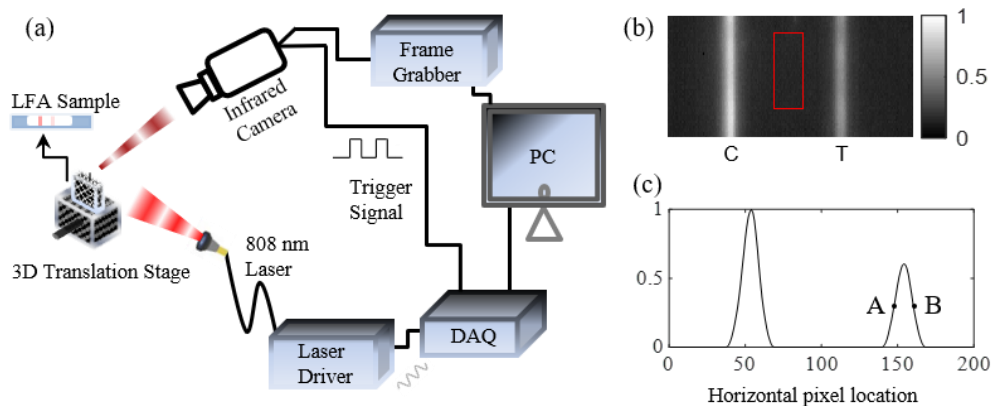


Figure 3.2. (a) A schematic diagram of the LIT imaging system used for the interpretation of LFA test strips. (b) Amplitude image after LIT measurement. (c) Average intensity of pixels over all the columns in a strip

### 3.3.4. Visual Interpretation of LFAs

Thirty-two students at York University, 20–35 years old, were recruited for visual interpretation of LFA strips spiked at various THC concentrations (0-25 ng/ml). Since LFA strips consisted of

colored test and control lines, the Ishihara color vision test was administered to each participant to screen for color vision deficiencies. Subjects were excluded if they did not pass the Ishihara color vision test and/or had any history of ocular disease/surgery. Two participants out of 32 could not pass the Ishihara color vision test, so they were excluded from the study. All participants had a normal or corrected-to-normal vision and reported no visual disorders or impairments. All studies were conducted in a room with normal lighting condition and participants were asked to perform two tasks. In the first task, participants were asked to interpret the test results, such as positive, negative and invalid in accordance with the LFA manufacturer instruction. The second task was focused on screening the ability of participants to sort LFAs based on the concentration of THC. To do so, two LFAs from each concentration of THC were randomly selected as reference visual guide for participants. These reference LFAs were represented to participants as bins. Only investigators were aware of the concentration of THC at each bin. In the following text, we will identify the bins as bins 1-6 corresponding to THC concentrations of 0, 2, 5, 7.5, 10 and 25 ng/ml, respectively. After the preparation of bins, visual assessments of participants were tested using the remaining 8 LFAs at each concentration. That is, the remaining 48 test LFAs (6 concentrations  $\times$  8 LFAs at each concentration) were shuffled and placed in a container. Then, participants were asked to pick up test LFAs one-by-one, compare the test LFA against all reference bins, then place the test LFA in the bin that they think best matches the test LFA. To minimize the subjective bias (memorization), the positions of the reference LFAs and corresponding bins were randomized 3 times (every 1/3 of the total LFAs) during each study. The test was repeated for all the spiked LFA test strips with all the 30 participants, resulting in 1,440 (48 $\times$ 30) data points. This study was approved by the office of the research ethics committee at York University (certificate #: e2019-006) and was conducted according to the Declaration of Helsinki.

### **3.3.5. Data Analysis**

The one-way analysis of variance (ANOVA) was used to determine whether there were any statistically significant differences in mean normalized amplitude values between different concentration groups. If the ANOVA showed a significant difference between the mean values, post-hoc pairwise comparisons were conducted to identify which pairs of means were

significantly different from each other. For the pair-wise comparison, a Tukey’s honestly significant difference (Tukey’s HSD) test was adopted.

To determine the detection performance metrics of visual interpretations, bin numbers were used for the criterion for determining true positive (TP), false positive (FP), true negative (TN) and false negative (FN) values as shown in Table 1. For example, setting criterion to bin 2 (i.e., 2ng/ml) implies that a THC concentration of more than 2 ng/ml should be considered as a positive reading. That is, if a 0 or 2 ng/ml LFA is placed in bins #1 or 2, then it is considered as TN; if such LFA is placed in any of bins #3-6 a FP reading is produced. Conversely, if LFA with concentration more than 2 ng/ml is placed in bins # 3-6 then it is considered as TP; however, if such LFA is placed in bin # 1 or 2 a FN reading is produced. Using these data, sensitivity, specificity, accuracy, positive predictive value (PPV) and negative predictive value (NPV) were calculated at each criterion as:

$$\begin{aligned} \text{Sensitivity} &= \frac{TP}{TP+FN} & \text{Specificity} &= \frac{TN}{TN+FP} \\ \text{Accuracy} &= \frac{TP+TN}{TP+FP+TN+FN} & \text{PPV} &= \frac{TP}{TP+FP} & \text{NPV} &= \frac{TN}{TN+FN} \end{aligned} \quad (3.3.1)$$

Table 3.1. Four possible outcomes: true positive (TP), true negative (TN), false positive (FP), false negative (FN) at different criterion/cut-off levels (i.e., bin numbers)

Criteria	LFA concentrations	LFA placed in bin numbers					
		1	2	3	4	5	6
1	0	TN	FP				
	2,5,7.5,10 & 25	FN	TP				
2	0 & 2	TN		FP			
	5,7.5,10 & 25	FN		TP			
3	0,2 & 5	TN			FP		
	7.5, 10 & 25	FN			TP		
4	0,2, 5 & 7.5	TN				FP	
	10 & 25	FN				TP	
5	0,2, 5,7.5 & 10	TN					FP
	25	FN					TP

To determine the detection performance metrics of LIT, 50% of the LFAs in each concentration were randomly selected as a training/calibration set, and the remaining 50% of the LFAs were

considered as a test set. The highest and lowest amplitude values of training set LFAs specified the range of bins in each concentration. After identifying bins, the amplitude value of a test LFA was compared to those of the bins at each concentration. A test LFA with amplitude value within the range of the bin was placed in the same concentration bin whereas the test LFA with amplitude value outside the range of the bin was considered to go to either higher or lower concentration bins; that is, if the amplitude was greater than that of the bin of the same concentration, then it was placed in the lower concentration bins while if the amplitude was lower than that of the bin then it was placed in the higher concentration bins. After assigning all LFAs to appropriate bins, TP, FP, TN, and FN values were calculated using the approach shown in Table 1.

A receiver operating characteristic curve (ROC curve) was plotted to compare the detection performances of visual and LIT interpretations in distinguishing between the LFAs with THC and LFAs with no THC. Thresholds used for plotting ROC were the 5 different criteria (i.e., detection threshold) as described in Table 3.1. The area under the ROC curve (AUC) that is considered as an effective measure of accuracy was also calculated for quantitative comparisons.

### **3.4. Results**

#### **3.4.1. Lock-In Thermography Interpretation of LFAs**

Figure 3a depicts visual and LIT images of 6 representative LFAs at various THC concentrations. A decrease in the signal at the test lines is observed with the increase in THC concentrations in both visual and LIT images. However, LIT images show a better change in contrast of the test line as the concentration of THC increases compared to the contrast change in visual images. In LIT images, the test line of 5ng/ml (if not also 2 ng/ml) can be visually differentiated from the test lines of higher concentrations; however, it is very difficult to make such differentiation in visual images. For quantitative analysis, the normalized amplitude metric discussed in section 3.3.2 was calculated for all LFAs. Figure 3.3b shows the normalized amplitude values obtained from the representative LFAs of Fig. 3a. The difference in the peak values of the curves at the test line is clearly observed for each pair of concentrations. To examine repeatability, the coefficient of variation (CV) was calculated using the 5 repeated measurements of each LFA. The CV is the ratio of the standard deviation and the overall mean,

usually expressed as a percentage [37]. The averaged CV obtained from all the LFAs at all different concentrations was 2.03%, demonstrating high repeatability of LIT measurements.

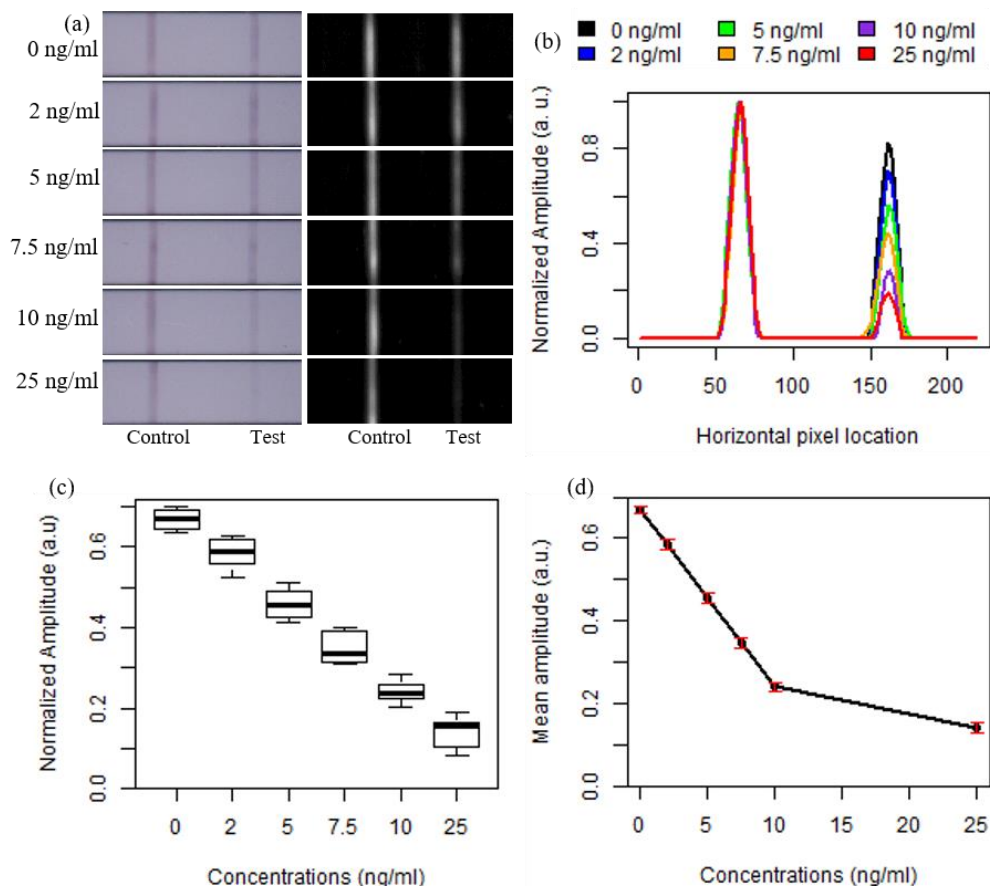


Figure 3.3. (a) Visual and LIT images of 6 representative LFAs at concentrations of 0, 2, 5, 7.5, 10 and 25 ng/ml. (b) Normalized amplitude values obtained from LIT LFA images in (a). (c) Distribution of the entire dataset of the LFAs at various concentrations obtained from the LIT system. (d) Mean normalized amplitude at different THC concentrations obtained from (c) with 99% confidence interval error bars.

Figure 3.3c displays the distribution of all the normalized amplitude values ( $n=300$ : 6 concentrations  $\times$  10 LFAs/concentration  $\times$  5 repeated measurement of each LFA). Each box shows the normalized amplitude values of the 50 measurements carried out at a given concentration. The box plot shows no overlap in the distribution of data between any two concentration groups. Accordingly, the mean normalized amplitude values with 99% confidence interval error bars (Figure 3.3d) show no overlap between any two concentration groups. One-way ANOVA test showed statistical significance between the mean normalized amplitude values of different concentration groups ( $p<0.001$ ). Tukey's pairwise comparisons showed that all the pairwise group comparisons were significantly different ( $p<0.001$ ). The effect size of 0.97 and

statistical power of 1.0 was obtained at a significance level of 0.01 using a sample size of 50 in each concentration group.

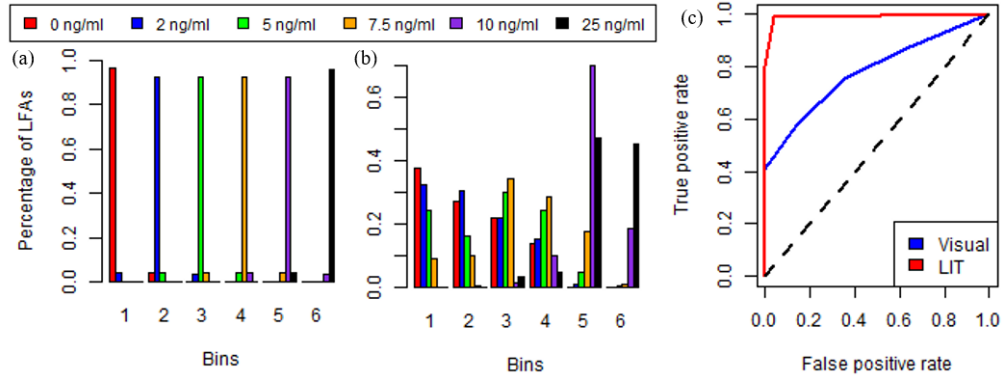


Figure 3.4. Percentage of LFAs of various concentrations dropped in bin number 1-6 in LIT (a) and visual interpretation (b). (c) ROC curves from the visual and LIT interpretation data.

Figure 3.4a shows the percentage of LFAs in each bin after splitting them into the training and test sets as described in Section 3.4.1. The sensitivity, specificity, accuracy, PPV, and NPV calculated from LIT data are shown in Table 3.1. The red solid line in Figure 3.4c represents the ROC curve plotted from the LIT data. The area under the ROC curve (AUC) was found to be 0.99.

Table 3.2. Sensitivity, specificity, accuracy, positive predictive value (PPV) and negative predictive value (NPV) calculated from the visual and LIT interpretation of LFAs at various criterion/cut-off.

Positive reading criterion (ng/ml)	Sensitivity		Specificity		Accuracy		PPV		NPV	
	LIT	Visual	LIT	Visual	LIT	Visual	LIT	Visual	LIT	Visual
$\geq 2$	0.96	0.68	0.96	0.38	0.96	0.53	0.96	0.52	0.96	0.54
$\geq 5$	0.96	0.60	1	0.65	0.98	0.62	1	0.63	0.96	0.62
$\geq 7.5$	0.96	0.47	1	0.86	0.98	0.66	1	0.77	0.96	0.62
$\geq 10$	0.97	0.88	1	1	0.98	0.94	1	1	0.97	0.90
$\geq 25$	0.96	0.45	1	1	0.98	0.73	1	1	0.96	0.65

### 3.4.2. Visual Interpretation of LFAs

Forty-eight spiked LFAs were interpreted by 30 participants, as described in Section 3.4.2. Figure 3.4b shows the percentage of LFAs of various concentrations dropped in bin numbers 1-6 by all 30 participants. The corresponding sensitivity, specificity, accuracy, PPV, and NPV are shown in Table 3.2. The solid blue plot in Figure 3.4c shows the ROC curve corresponding to the visual interpretation data. The area under the ROC curve was found to be 0.78.

### 3.5. Discussion and Conclusion

In this study, LFA strips for THC saliva test were spiked at various concentrations of THC and inspected visually by adults and a LIT imaging system. Figure 3.3a depicts visual images of 6 representative LFAs at various concentrations. At high THC concentrations (e.g., 25 ng/ml), THC binds effectively with the antibodies present in the LFA sample pad; therefore, the antigen immobilized at the test line is unable to restrain with antibody conjugate, preventing the GNPs from being fixed on the test line and yielding lack of signal at the test line. However, at lower THC concentrations (e.g., between 2 and 10 ng/ml), some of the antibody conjugates are able to bind with antigen immobilized at the test line, thus forming a faint test line. At low THC concentrations (e.g., less than 7.5 ng/ml) the change in contrast with the decrease of concentration becomes small, making the classification of LFA with THC and without THC challenging. Accordingly, in visual interpretation (Figure 3.4b) participants could not find the difference between the LFAs of concentrations less than 10 ng/ml; however, their diagnostic performance increased for LFA concentrations 10 ng/ml and higher. This indicates that THC concentrations of 10 ng/ml and 25 ng/ml were determined as a positive test by participants with higher accuracy. The sensitivity, specificity and accuracy values for identifying THC concentrations of 10ng/ml and more are 0.88, 1 and 0.94, respectively (Table 3.2). However, these values are less than 80% for identifying concentration less than 10 ng/ml and, as such, could not meet the Driving Under Influence of Drugs, Alcohol and Medicines (DRUID) standard of >80% sensitivity, specificity and accuracy at nominal detection threshold [38]. Similarly, PPV (i.e. probability of a positive reading being correct) and NPV (i.e. probability of a negative reading being correct) are crucial indicators of performance for a drug screening device at the roadside and workplace. These values are less than 80% for identifying THC concentrations of less than 10 ng/ml for visual interpretation. Therefore, based on the results depicted in Table 3.2 one can assume a detection

threshold of 10ng/ml for visual interpretation of LFAs using in this study. We, however, anticipate this visual interpretation detection performance and threshold to deteriorate in practice because our participants were visually healthy young adults (20-35 years) with no history of eye surgery, color blindness, and visual impairment but at roadside or workplace tests are usually interpreted by individuals of different ages. Furthermore, since our visual tests were conducted in a well-illuminated room, we anticipate that the reliability of visual interpretation results to decline in practice due to suboptimal lighting conditions, such as roadside conditions at nighttime or in bad weather. Therefore, visual interpretation results suggest that if LFAs are interpreted by an objective and unbiased reader at roadside, detection of THC concentrations at *per se* limit (~1-5 ng/ml) is extremely unlikely and that one should expect inconsistent and unreliable readings when THC concentrations are above *per se* limit but lower than 10 ng/ml (if not 25 ng/ml).

Figure 3.3a depicts LIT images of 6 representative LFAs at various concentrations. Qualitative analysis of these images (Fig 3b) suggests that, unlike visual images, the contrast of the test line in LIT is very sensitive to change in THC concentration. Better sensitivity of LIT can be attributed to the fact that LIT utilizes the diffusion of thermal waves to interrogate the entire thickness of LFAs whereas the scattered light in visual interpretation originates predominantly from surface (and superficial layer) of LFA [31]. That is, in LIT the contributions of all the GNPs located within the thermal diffusion length are integrated and accounted for in the normalized amplitude values. Fig. 3d depicts the mean normalized amplitude values within the test band for stripes with different THC concentrations. The mean normalized amplitude value decreases monotonically with an increase in the THC concentrations in the sample. The mean normalized amplitude values were statistically different ( $p < 0.001$ ) between all the THC concentrations used in this study. The post-hoc pair-wise comparison shows that the LIT can reliably differentiate LFA spiked at 2 ng/ml from those spiked at 0 ng/ml. Table 3.2 shows that LIT technology can differentiate THC concentrations of 2 ng/ml and more from 0 ng/ml with sensitivity, specificity, and accuracy of 96% that is considerably higher than the standard set by DRUID for nominal detection threshold of a drug screening device [38]. Also, the predictive values (i.e. PPV and NPV) are almost 100% at 2 ng/ml which implies the outstanding confidence that one can have in LIT technology results. These experimental results and statistical analyses suggest that interrogation of the thermal signature of GNPs from the entire thickness of the LFAs

significantly improves the detection threshold of commercially available LFAs (2 ng/ml vs. the nominal 25 ng/ml limit).

The area under the ROC curve plotted from the LIT data is considerably higher than that of the visual interpretation data (0.99 vs 0.78). This indicates that the diagnostic performance of LIT is better than visual interpretation for distinguishing LFAs spiked with THC and without THC. Another interesting aspect of the developed LIT system is its potential for quantifying THC concentration. Since the box plots of any two concentrations do not overlap (Fig 3c), this imaging modality can use data of Figure 3.3c as calibration to provide an accurate prediction for THC concentration in oral fluid.

The performance can be improved even more by adopting better lateral flow immunoassay assembly approaches. As can be seen in Figure 3.3c, there is a high degree of variability among the LFAs of the same concentrations. This may be due to the batch processing approach used in the LFA assembly. The batch processing approach involves a high degree of manual labor and can be prone to product variability [39]. Another approach for improving performance is the use of a green laser beam (wavelength  $\sim 550$  nm) instead of the near-infrared laser (808nm). Our spectral measurements show that the difference in the absorption of light between the test line and the surrounding nitrocellulose paper is maximum at a wavelength of 550 nm. However, the shorter-wavelength lasers are typically more expensive and hence not suitable for commercialization. We are currently exploring the replacement of the 808nm laser with an assembly of high-power green LEDs.

In conclusion, we have developed a lock-in thermography imaging system to demonstrate the detection and quantification of THC in the oral fluid at unprecedented low concentrations. Our results suggest that LIT interrogation of low-cost commercial LFAs allows for more than an order of magnitude improvement in the detection threshold. We have also compared the performance of our LIT reader with visual interpretation. Results suggest a significant improvement in detection threshold and accuracy when using LIT. Based on the DRUID definition of detection threshold, the detection threshold of visual interpretation in our study is 10 ng/ml with 94% accuracy whereas the detection threshold of LIT is 2 ng/ml at 96% accuracy. The 2ng/ml detection threshold of developed LIT technology is significantly better than any of the workplace or roadside on-site THC screening solutions currently available in the market

(e.g., Dräger DrugTest®). We are currently pursuing commercialization of the developed technology and anticipate it to be used in testing cannabis consumption in various application fields, such as testing (a) drivers in the roadside for investigating driving under the influence of cannabis and drug-related accidents (b) employees to ensure workplace safety (c) patients in hospitals who uses cannabis for pain relief and/or sleep improvement (d) players in competitions who uses cannabis to enhance athletic performance (e) correlation of THC with human cognitive and motor functions and (f) cannabis manufacturing plans for quality control purposes. Besides the detection of THC, LFAs are routinely used for the detection of pathogenic bacteria in food and water [40-41], disease biomarkers such as foot-and-mouth disease virus [42], extra parenchymal neurocysticercosis [43], and cancer and cardiac markers in various biofluids. Since a significant majority of LFAs are based on GNPs, the developed LIT reader can potentially be used for sensitive and quantitative interpretation of results in such delicate application. The most important limitation of our thermo-phonic system is the cost and size of instrumentation. The cost of our system is mostly determined by the cost of the infrared camera (approximately \$7,000 USD for the camera used in this study). However, we have recently shown that the cost and size limitation can be significantly reduced by using cell-phone attachment infrared cameras [44]. Development of a portable system using low-cost (\$250) cell-phone attachment infrared cameras for the detection and quantification of THC in oral fluid is in progress in our lab. We anticipate that the low-cost and portable thermo-phonic imager promises an affordable solution that allows for proper enforcement of *per se* regulations worldwide.

### 3.6. References

1. Public Safety Canada. Cannabis Policy Performance Metrics, Research Summary 2016, Ottawa, Ontario.
2. World Health Organization Reports. *Management of substance abuse: Cannabis*. [https://www.who.int/substance\\_abuse/facts/cannabis/en/](https://www.who.int/substance_abuse/facts/cannabis/en/).
3. W. C. Kerr, Y. Ye, M. S. Subbaraman, E. Williams, & T. K. Greenfield, *Journal of studies on alcohol and drugs*, 79(3), 495-502 (2018).
4. Shikha Prashad and Francesca M. Filbey. “Cognitive motor deficits in cannabis users.” Feb. 2017. Current Opinion in Behavioral Sciences.
5. Sewell, Poling, and Sofuoglu. See also: Brooks-Russell, Wempe, Vigil, et al. “Marijuana use and driving: Systematic literature review.” 2017. Colorado Department of Public Health and Environment.
6. Ole Rogeberg and Rune Elvik. “The effects of cannabis intoxication on motor vehicle collision revisited and revised.” Feb. 2016. Addiction.

7. Jean-Louis Martin, Blandine Gadegbeku, Dan Wu, et al. "Cannabis, alcohol, and fatal road accidents." 2017. PLoS One. In comparison, the study found that drivers under the influence of alcohol are 17.8 times more likely to be culpable for a fatal accident.
8. European Monitoring Centre for Drugs and Drug Addiction (2019), European Drug Report 2019: Trends and Developments, Publications Office of the European Union, Luxembourg
9. Canadian Centre on Substance Use and Addiction 2018, "Canadian drug summary: cannabis"
10. European Monitoring Centre for Drugs and Drug Addiction, "The state of the drugs problem in Europe" Annual report 2012.
11. D. J. Beirness & A. J. Porath-Waller, "Clearing the smoke on cannabis: Cannabis use and driving-an update," Canadian Centre on Substance Abuse" (2019).
12. Substance Abuse and Mental Health Services Administration, "The National Survey on Drug Use and Health: 2017"
13. Australian Institute of Health and Welfare 2017. National Drug Strategy Household Survey 2016: detailed findings. Drug Statistics series no. 31. Cat. no. PHE 214. Canberra: AIHW
14. R. L. Hartman, T. L. Brown, G. Milavetz, A. Spurgin, D. A. Gorelick, G. R. Gaffney, & M. A. Huestis, "Effect of blood collection time on measured  $\Delta^9$ -tetrahydrocannabinol concentrations: implications for driving interpretation and drug policy," *Clinical chemistry*, 62(2), 367-377 (2016).
15. D. J. Beirness, & D. R. Smith, "An assessment of oral fluid drug screening devices," *Canadian Society of Forensic Science Journal*, 50(2) (2017).
16. M.A. Huestis, E. J. & Cone, "Relationship of  $\Delta^9$ -Tetrahydrocannabinol Concentrations in Oral Fluid and Plasma after Controlled Administration of Smoked Cannabis," *Journal of analytical toxicology* 28, 394-399, (2004).
17. G. Li, S. P. Baker, Q. Zhao, J. E. Brady, B. H. Lang, G. W. Rebok, & C. DiMaggio "Drug violations and aviation accidents: findings from the US mandatory drug testing programs," *Addiction*, 106(7), 1287-1292 (2011).
18. M. T. French, M. C. Roebuck, & P. K. Alexandre, "To test or not to test: do workplace drug testing programs discourage employee drug use?" *Social science research*, 33(1), 45-63 (2004).
19. S. George, "A snapshot of workplace drug testing in the UK," *Occupational Medicine*, 55(1) (2005).
20. O. A. Silva, & M. Yonamine, Drug abuse among workers in Brazilian regions. *Revista de saúde pública*, 38(4), 552-556 (2004).
21. E. J. Cone, L. Presley, M. Lehrer, W. Seiter, M. Smith, K.W. Kardos, D. Fritch, S. Salamone & R. S. Niedbala, "Oral fluid testing for drugs of abuse: positive prevalence rates by Intercept™ immunoassay screening and GC-MS-MS confirmation and suggested cutoff concentrations," *Journal of analytical toxicology*, 26(8), 541-546 (2002).
22. S. Macdonald, W. Hall, P. Roman, T. Stockwell, M. Coghlan, & S. Nesvaag, "Testing for cannabis in the work-place: a review of the evidence," *Addiction*, 105(3), 408-416 (2010).
23. H. Choi, S. Baeck, E. Kim, S. Lee, M. Jang, J. Lee, H. Choi, & H. Chung, "Analysis of cannabis in oral fluid specimens by GC-MS with automatic SPE," *Science & Justice*, 49(4), 242-246 (2009).
24. M. Sánchez, A. Arroyo, M. Barbal, M. Palahí, & A. Mora, "Cozart® RapiScan Oral Fluid Drug Testing System validation by GC-MS/MS analysis," In *Annales de Toxicologie Analytique*, 20(3), 131-136 (2008).

25. V. Reinstadler, S. Lierheimer, M. Boettcher, & H. Oberacher, "A validated workflow for drug detection in oral fluid by non-targeted liquid chromatography-tandem mass spectrometry," *Analytical and bioanalytical chemistry*, 411(4), 867-876 (2019).
26. O. Quintela, D. M. Andrenyak, A. M. Hoggan, & D. J. Crouch, "A validated method for the detection of  $\Delta^9$ -tetrahydrocannabinol and 11-nor-9-carboxy- $\Delta^9$ -tetrahydrocannabinol in oral fluid samples by liquid chromatography coupled with quadrupole-time-of-flight mass spectrometry," *Journal of analytical toxicology*, 31(3), 157-164 (2007).
27. D. J. Crouch, J. M. Walsh, L. Cangianelli, O. Quintela, "Laboratory evaluation and field application of roadside oral fluid collectors and drug testing devices," *Ther. Drug Monit.* 30, 188-195(2008).
28. B. D. Plouffe, S. K. Murthy, "Fluorescence-based lateral flow assays for rapid oral fluid roadside detection of cannabis use," *Electrophoresis* 38, 501-506 (2017).
29. P. Rezai, N. Tabatabaei, and A. Ojaghi. "System and method for photo-thermal analysis of immunoassay tests." U.S. Patent Application 15/839,325, filed May 23, 2019.
30. K.M. Koczula, & A. Gallotta, Lateral flow assays. *Essays in biochemistry*, 60(1), 111-120 (2016).
31. A. Ojaghi, M. Pallapa, N. Tabatabaei, and P. Rezai, "High-sensitivity interpretation of lateral flow immunoassays using thermophotonic lock-in imaging," *Sensors and Actuators A: Physical*, 273, 189-196 (2018).
32. Canadian Society of Forensic Science Drugs and Driving Committee (DDC) Drug Screening Equipment – Oral Fluid Standards and Evaluation Procedures.
33. N. Tabatabaei, A. Mandelis, and B. T. Amaechi, "Thermophotonic lock-in imaging of early demineralized and carious lesions in human teeth," *J. Biomed. Opt.* **16**, 071402 (2011).
34. N. Tabatabaei, A. Mandelis, M. Dehghany, K. H. Michaelian, and B. T. Amaechi, "On the sensitivity of thermophotonic lock-in imaging and polarized Raman spectroscopy to early dental caries diagnosis," *J. Biomed. Opt.* **17**(2), 025002 (2012).
35. A. Ojaghi, A. Parkhimchyk, and N. Tabatabaei, "First step toward translation of thermophotonic lock-in imaging to dentistry as an early caries detection technology," *J. Biomed. Opt.* **21**(9), 096003 (2016).
36. E. B. Shokouhi, M. Razani, A. Gupta, & N. Tabatabaei, "Comparative study on the detection of early dental caries using thermo-photonic lock-in imaging and optical coherence tomography," *Biomedical optics express*, 9(9), 3983-3997 (2018).
37. J. M. Bland, D. G. Altman, "Statistical notes: measurement error proportional to the mean," *BMJ*, 313(7049):106, 1996.
38. M. Marillier and A. G. Verstraete, "Driving under the influence of drugs," *WIREs Forensic Sci*, 2019; 1: e1326
39. Innova Biosciences Ltd, A guide to lateral flow immunoassays, Babraham Research Campus, Cambridge.
40. Y. Zhao, H. Wang, P. Zhang, C. Sun, X. Wang, X. Wang, R. Yang, C. Wang, L. Zhou, "Rapid multiplex detection of 10 foodborne pathogens with an up-converting phosphor technology-based 10-channel lateral flow assay," *Sci. Rep.* 6 (2016).
41. J. Hwang, D. Kwon, S. Lee, and S. Jeon, "Detection of Salmonella bacteria in milk using gold-coated magnetic nanoparticle clusters and lateral flow filters," *RSC Adv.* 6(54), 48445-48448 (2016).

42. K.O. Jae, N. P. Ferris, K. N. Lee, Y. S. Joo, B.H. Hyun, and J.H. Park, “Simple and rapid lateral-flow assay for the detection of foot-and-mouth disease virus, *Clin.Vaccine Immunol.* 16, 1660–1664 (2009).
43. A. Fleury, P. Sastre, E. Sciutto, S. Correia, A. Monedero, A. Toledo, M. Hernandez, L.J.S. Harrison, & R.M.E. Parkhouse, “A lateral flow assay (LFA) for the rapid detection of extraparenchymal neurocysticercosis using cerebrospinal fluid, *Exp. Parasitol.* 171, 67-70 (2016).
44. M. Razani, A. Parkhimchyk, & N. Tabatabaei, “Lock-in thermography using a cellphone attachment infrared camera,” *AIP. Advances*, 8(3), 035305 (2018).

## CHAPTER FOUR

### **Low-Cost Active Thermography using Cellphone Infrared Cameras: from Early Detection of Dental Caries to Quantification of THC in Oral Fluid**

Nakisa Samadi<sup>+</sup> (co-first author), Damber Thapa<sup>+</sup> (co-first author), Mohammadhossein Salimi, Artur Parkhimchyk, and Nima Tabatabaei<sup>\*</sup>

Department of Mechanical Engineering, Lassonde School of Engineering, York University

<sup>+</sup>these authors contributed equally to this work

*Note: This chapter is a modified version of the published paper*

#### **4.1. Abstract**

Active thermography (AT) is a widely studied non-destructive testing method for the characterization and evaluation of biological and industrial materials. Despite its broad range of potential applications, commercialization and wide-spread adaption of AT has long been impeded by the cost and size of infrared (IR) cameras. In this paper, we demonstrate that this cost and size limitation can be overcome using cell-phone attachment IR cameras. A software development kit (SDK) is developed that controls camera attributes through a simple USB interface and acquires camera frames at a constant frame rate up to 33 fps. To demonstrate the performance of our low-cost AT system, we report and discuss our experimental results on two high impact potential applications. The first set of experiments is conducted on a dental sample to investigate the clinical potential of the developed low-cost technology for detecting early dental caries, while the second set of experiments is conducted on the oral-fluid based lateral flow immunoassay to determine the viability of our technology for detecting and quantifying cannabis consumption at the point-of-care. Our results suggest achievement of reliable

performance in the low-cost platform, comparable to those of costly and bulky research-grade systems, paving the way for translation of AT techniques to market.

## 4.2. Introduction

Over the past four decades, the notion of non-radiative conversion of light energy into heat energy (photothermal sciences) has made remarkable achievements in the development of metrology and imaging techniques in the fields of basic sciences, engineering, and medicine [1]. Many of such techniques utilize infrared (IR) thermography for detection of materials' defects, or tissue malignancies, through interrogation of thermal radiations emitted from specimens in response to external excitations (aka. active thermography) [2]. The role of external excitation (normally optical excitation) in active thermography (AT) is to enable reliable detection of an *a priori* known waveform in the highly noisy thermal radiation signals of specimens. In the presence of defects, the thermal impedances introduced by defects alter the induced local temperature field which in return alters the amplitude and phase of the *a priori* known radiative signals captured from defective regions. Consequently, the demodulation of IR radiative signals enables the detection of defective regions with sharp contrast and high signal-to-noise ratio (SNR).

Based on the temporal pattern of external excitation, AT techniques can be categorized into pulsed thermography, lock-in thermography (LIT), and matched-filter thermography. In pulsed thermography, the sample is excited by a short pulse of light, usually a flash lamp, and the transient surface temperature profile is, subsequently, recorded by a thermal camera and then analyzed [3]. In LIT, on the other hand, a single-frequency intensity-modulated external excitation (e.g., laser) is utilized to generate a steady-state modulated temperature field (aka thermal-wave field) inside the sample while recording the sample temporal temperature responses with an IR camera [4-6]. A key shortcoming of both pulsed and LIT is the inherent compromise between inspection depth and depth resolution [2]. That is, in both methods, inspecting deep into the sample comes at the price of deterioration of the resolution of the imaging system due to the diffuse nature of thermal waves. To alleviate this shortcoming, recently, matched-filter thermography has been introduced as the photothermal analog of optical coherence tomography (OCT) [7-11]. In matched-filter thermography methods, radar pulsed-

compression techniques, such as linear frequency modulation [7-8] or binary phase coding [9], are used for the external excitation in order to improve system point spread function to achieve depth-resolved and “crisp” images from an intrinsically diffuse thermal-wave field.

The non-contact and non-ionizing nature of AT, as well as its tunability to probe a broad range of materials (e.g., opaque [12-16], turbid/biological [17-19]) using different types of excitation sources (e.g., optical [18], magnetic [13], mechanical waves [15], electrical [12, 20] or even cyclic stress/strain [14]), have resulted in the widespread adoption of AT in non-destructive testing research and development. For example, AT techniques have been widely utilized by researchers for inspection of industrial samples for detection of damages in Carbon Fiber Reinforced Plastic (CFRP) materials [21], inspection of airplane parts [22] and detection of electric leakages in integrated circuits [20]. More recently, AT has been utilized to detect malignancies in human hard and soft tissues such as early detection of demineralization in dental enamel [17-19], cutaneous melanoma [23], mineral loss in bone [24] or tumors [25].

Despite the abovementioned broad range of applications, commercialization and wide-spread adoption of these techniques by industry have been significantly impeded by the cost and the size of IR cameras used in active thermography. IR cameras suitable for thermal measurements are either mid-wavelength (MWIR: 3-5  $\mu\text{m}$ ) or long-wavelength (LWIR: 8-14  $\mu\text{m}$ ) cameras, measuring sample temperature based on objects’ thermal/Planck radiation [26]. MWIR cameras typically use sensitive photon detectors but need dedicated cooling systems which result in higher size, cost, weight, and complexity of the imaging system. LWIR cameras, on the other hand, use less sensitive uncooled microbolometer thermal detectors and can be produced at a lower cost compared to MWIR cameras [27-28]. In general, the price of research-grade thermal cameras, depending on the type (MWIR vs LWIR), number of pixels, objective focal length and F-number ranges between \$10k-\$200k, posing a key barrier to commercialization of AT technologies. In an attempt to overcome this barrier, we recently demonstrated the possibility of incorporating low-cost (~\$250) and small cell-phone attachment LWIR camera instead of the costly research-grade IR cameras for performing AT [29]. In that initial work [29], the performance of the developed LIT system was limited by the slow and inconsistent frame rate of the camera (~15 fps) as well as the disruptions in the image acquisition due to frequent execution of cell-phone attachment camera’s native calibration and non-uniformity correction procedures.

Here in this manuscript, we report on the development of a reliable software development kit (SDK) which not only enables control of camera attributes but also offers reliable acquisition of frames at constant frame rates of up to 33 fps through a simple USB interface. To demonstrate the feasibility of conducting reliable AT with a low-cost cellphone IR camera, in sections below, after discussing the significance of performing LIT at high frame rates, we present and discuss our experimental results on two high impact areas of detecting early stages of demineralization in human dental enamel and detection and quantification of cannabis in oral fluid.

### **4.3. Results and Discussions**

**Evaluation of SDK and developed low-cost LIT system performance:** To study the advantages and limitations of developed SDK platform over manufacturer's software, comparative LIT experiments were carried out using the IR camera frames captured via developed SDK and those directly captured by the SEEK APP (Seek Thermal Inc.; Santa Barbara, CA) hosted on an Android Google Pixel 4 cellphone. LIT experiments were carried out on a thick Aluminum block (40mm×30mm×30mm) interrogated at a laser modulation frequency of 1Hz to compare the maximum frame rates and consistency of image acquisitions. Figures 1a and 1b show sections (10 sec) of the time-laps signals from the central pixel of the camera captured via manufacturer applet and developed SDK, respectively. These oscillations of surface temperature are the thermal waves recorded from the sample surface of a semi-infinite opaque body. Evaluation of these signals suggests periodic disruptions in the recording of the surface thermal wave by manufacturer's software due to periodic execution of a non-uniformity correction routine, red dashed rectangle in Figure 4.1 (a). Signals captured by developed SDK, on the other hand, are continuous and without any disruption, resulting in the proper realization of the 1Hz modulation frequency of the thermal-wave, Figure 4.1 (b). The maximum achievable frame rate is also significantly larger (33Hz vs 9 Hz) with the SDK. Figures 4.1(c) and 1(d) show the spectra of the recorded waveforms in the Fourier domain. These spectra suggest that the presence of disruptions in the acquisition of frames by manufacturer software results in the appearance of erroneous frequency components in the frequency domain, while the spectrum of the signal acquired by developed SDK shows a single dominant peak at the modulation frequency of the laser. The inconsistent and slower frame acquisition with manufacturer software

also results in lower SNR of recorded thermal-waves. The SNRs for the signals obtained under identical experimental conditions using manufacturer software and developed SDK were found as 54.55 dB and 83.41 dB, respectively (using equation (1); Methods section). These qualitative and quantitative comparisons of quality of signals suggest the superior and reliable performance of developed SDK, paving the way for the development of low-cost, yet reliable, AT systems and their commercialization. We intend to offer the developed SDK to the scientific and educational communities at no charge and in the context of collaboration; therefore, entities interested in using the SDK are urged to contact us.

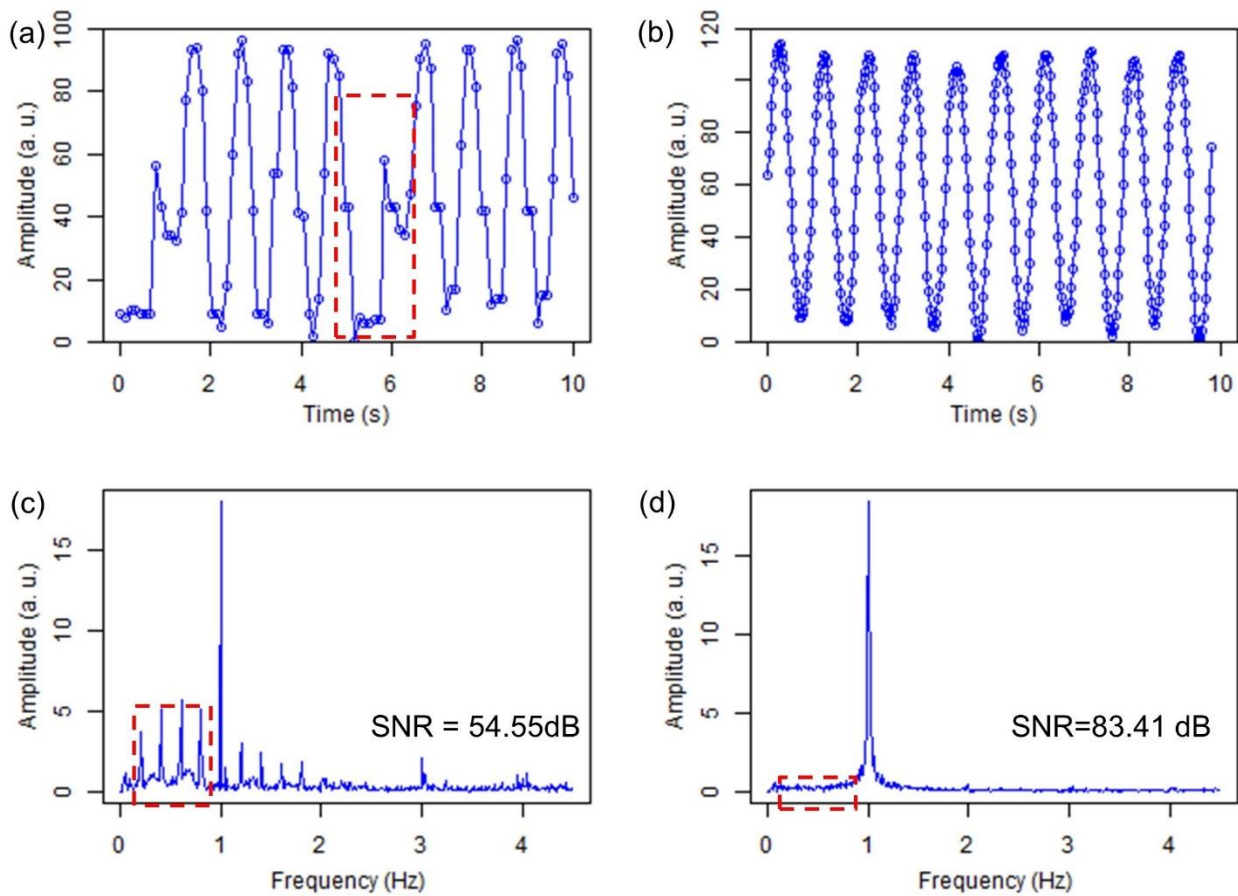


Figure 4.1. Temporal variations of surface temperature captured by (a) the SEEK THERMAL app and (b) developed SDK. (c) and (d) are Fourier spectrums of (a) and (b), respectively. Red rectangle in (a) shows acquisition disruptions in manufacturer’s software. Red rectangles in (c) and (d) are spectral ranges considered as noise for calculating SNR.

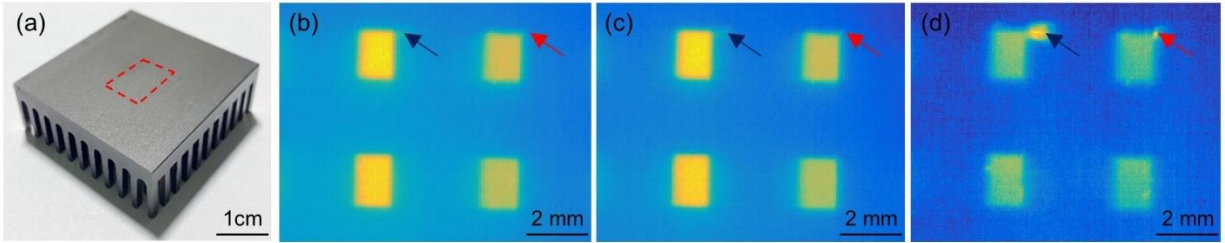


Figure 4.2. (a) Photograph of a thermal heat sink; red dashed rectangle depicts the imaging area. LIT Amplitude image of the area of heat sink with four pin-fins below interrogated surface (yellow rectangles) imaged at modulation frequency with camera frame rates of (b) 9 fps and (c) 33 fps. (d) LIT Amplitude image at a modulation frequency of 10Hz and camera frame rate of 33 Hz, demonstrating the possibility of resolving small defects with the improved resolution at higher modulation frequencies with high frame rates.

As shown in Figure 4.1, the developed SDK allows for enhancement of the acquisition rate from 9 fps to 33 fps. One of the benefits of having a higher frame rate in LIT is that it enables proper sampling of higher frequency thermal waves based on the Nyquist–Shannon sampling theorem. LIT at higher modulation frequencies results in shortening of thermal diffusion length. This shortening, in return, leads to improvement of image resolution, enabling the detection of smaller defects. To demonstrate this added value experimentally, we conducted LIT experiments on a pin-fin thermal heat sink, Figure 4.2a. The size of the heat sink is  $40.6\text{mm} \times 40.6 \times 13.3\text{mm}$  and consists of pin fins of cross-section size  $1.4\text{mm} \times 2.4\text{mm}$  at 2 mm beneath top plate. Figure 4.2b and 2c show LIT amplitude images at a modulation frequency of 1Hz at frame rates of 9 fps and 33 fps, respectively. These images clearly show the location and size of the subsurface fins. However, no manufacturing defect can be resolved at the connection sites between fins and plate based on images at 1Hz modulation frequency, not even at 33 fps. Figure 4.2d is a LIT amplitude image at a laser modulation frequency of 10Hz with a frame rate of 33fps; note that the native camera frame rate of 9 fps cannot sample a 10Hz thermal wave according to Nyquist–Shannon sampling theorem. The advantage of higher frame rate and higher modulation frequency is clearly seen in the 10Hz amplitude image. Small connection defects in the top two fins (arrows) can clearly be resolved due to the reduction of thermal diffusion length and corresponding improvement of resolution at the higher modulation frequency.

Another key advantage of higher frame rates in LIT is improvement in signals' SNR that eventually translates to an improvement in LIT images quality and reliability. To demonstrate this concept experimentally, we carried out LIT experiments with the developed system at frame

rates of 9, 15 and 33 fps, corresponding to the nominal frame rate of Seek thermal camera, results published in our previous work [29] and the current imaging system, respectively. In these experiments, the sample was an Aluminum block (45mm×25mm×30mm) that had three drilled subsurface holes of the diameter of 5mm, simulating circular defects 300μm, 500μm and 800μm below the intact interrogation surface, as shown schematically in Figure 4.3a. The laser beam was intensity-modulated at 1Hz and covered a circular area on the sample surface with a diameter of 2 cm. To test the repeatability, experiments were repeated 3 times for each subsurface hole at each frame rate and average normalized root-mean-square deviation (NRMSD: equation (2); Methods section) was calculated. The NRMSD is one commonly used quantitative measure of the deviations of repeated measurements from the mean value. In Figure 4.3, panels b1-b3 depict the LIT amplitude images obtained from the shallowest defect (300μm) at camera frame rates of 9, 15 and 33 fps, respectively. Similarly, panels c1-c3 and panels d1-d3 show images of defects 500μm and 800μm below surface, respectively. The dashed circle in all images indicates the true location and size of the subsurface holes. In these images, the defective area (hole) can be realized in amplitude images as a region of higher amplitude, confirming additional diffusive contributions of thermal energy to sample surface as a result of the introduction of thermal impedance by the defect. These observations are consistent with those obtained in our previous benchmark tests using expensive research-grade IR cameras [7, 30-31]. While defects can be detected in all 3 frame rates, the defect contrast, and consequently reliability of defect detection, is directly correlated with an increase in the frame rate. The true size of the holes is better recognized in the amplitude image obtained at higher frame rates. To quantitatively compare the images at different frame rates, pixels inside the circles were extracted and analyzed. Panels b4, c4, and d4 depict the mean and standard deviation (STD) of pixels inside circular defective regions for the 300μm, 500μm and 800μm subsurface holes, respectively. For a given hole, the mean intensity increases, while the STD decreases, as the frame rate increases. However, the mean values were not significantly different among different frame rates for a given hole (Kolmogorov-Smirnov normality test followed by Paired t-test  $p>0.05$ ,  $n=3$  repeated experiments for each hole). Nevertheless, the effect of frame rate on image quality metrics was significant: contrast-to-noise ratio (CNR) and mean-to-standard-deviation ratio (MSR) were calculated from the amplitude images: MSR measures the smoothness of regions and is calculated from the regions that have a homogeneous appearance. The CNR, on

the other hand, measures the contrast between the foreground and background regions, representing the ability to visualize the defect in the image through the noise. The table in panel (e) depicts the MSRs and CNRs values computed from the amplitude images at 3 different frame rates. The STDs were calculated from 3 repeated experiments in each hole at each frame rate. This table demonstrates a considerable improvement of both MSR and CNR by increasing the LIT system camera frame rate. The paired t-test shows that CNR is significantly increased ( $p < 0.05$ ) with the increased frame rate in all the pairwise comparisons, except 15 fps vs. 33 fps and 9 fps vs. 15 fps with 500 $\mu\text{m}$  hole and 15 fps vs. 33 fps with 800 $\mu\text{m}$  hole. Similarly, MSR significantly increased ( $p < 0.05$ ) with the increase in frame rate in all the pairwise comparisons, except 9fps vs. 15 fps with hole 500 $\mu\text{m}$  and 800 $\mu\text{m}$ . These statistical analyses indicate that LIT with developed SDK at 33fps results in significantly better MSR and CNR compared to those obtained at native camera frame rate (i.e., 9fps). Moreover, the average NRMSD decreases with increasing the frame rate indicating better repeatability with the higher frame rate. The averaged NRMSD, at a given frame rate, increases with increasing depth of the defect due to the degradation of signals' SNR from deeper holes as a result of the damped and diffuse nature of thermal waves. The histograms of the amplitude image values from the defect and background regions at camera frame rates of 9, 15 and 33 fps for the three holes are included in Supplementary Figure 4.7. These histograms, also, demonstrate the reduction of distributions' STD (Supplementary Table 4.1) with the increase in frame rate which, from a statistical point of view, translates to improvement in the reliability of defect detection.

The results of aluminum samples demonstrate the importance and significance of having higher frame rates in LIT, especially in a low-cost system that is prone to noise. Moreover, an increase of frame rate in LIT platforms extends the range of applications of LIT systems by enabling proper sampling of higher frequency thermal waves that are required for interrogation of thinner samples (e.g., coatings) and/or smaller defects in accordance to the concept of thermal-diffusion length. It should, however, be noted that conducting AT at higher frame rates results in acquisition of more data and require more computing power, which can become problematic if data analyses are to be carried out by personal portable devices like cellphones. Utilizing real-time lock-in processing algorithms instead of fast Fourier transform or performing data analyses with more powerful tablets are few approaches for overcoming this potential limitation.

To demonstrate the potential impact of the development of reliable, yet low-cost, LIT systems, sections below depict experimental results obtained by our developed system in high impact areas of detection of human early dental caries and detection and quantification of cannabis consumption from oral fluids.

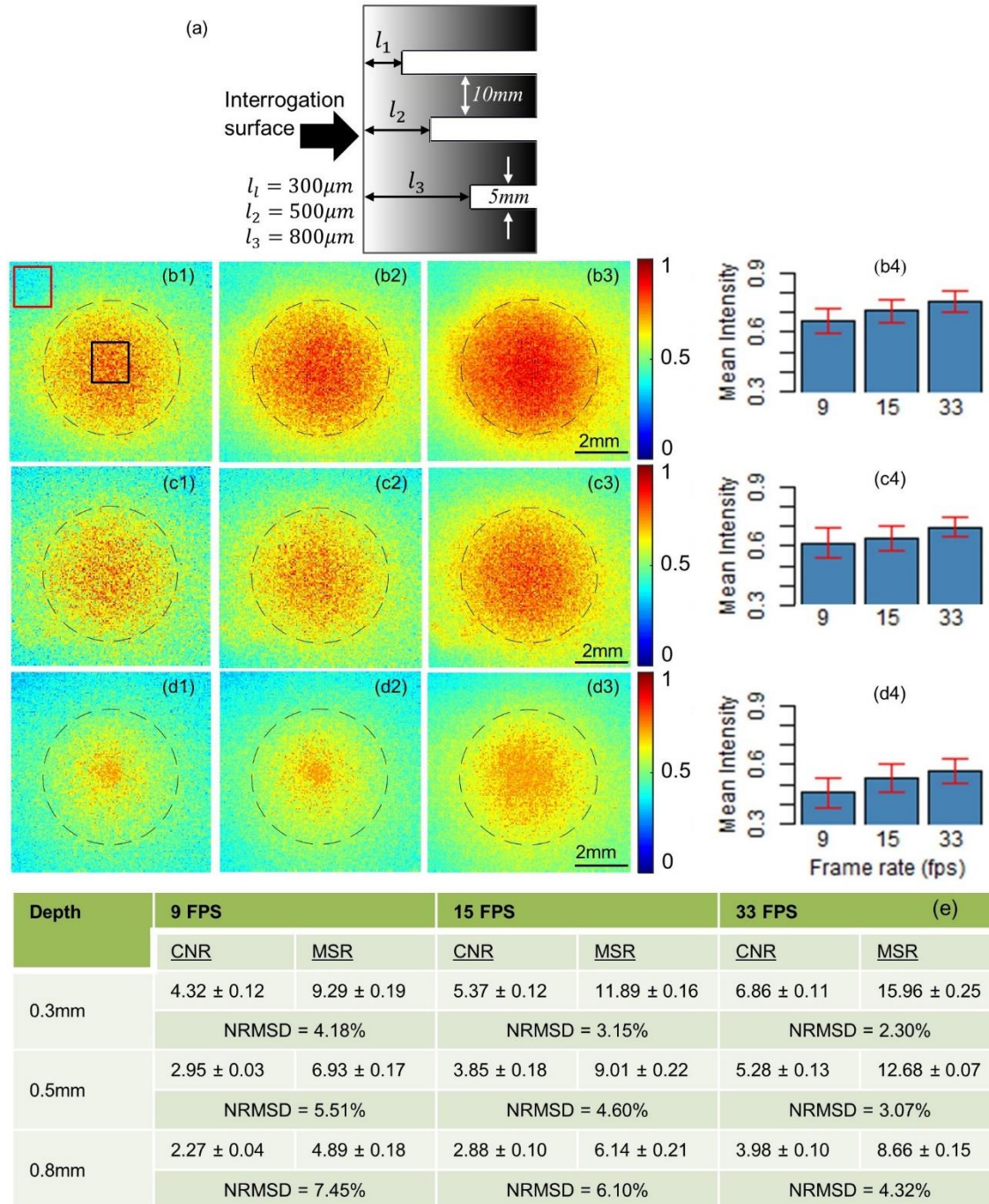


Figure 4.3(a) A schematic diagram of the cross-section of the block with a blind hole at 300 $\mu\text{m}$ , 500 $\mu\text{m}$ , and 800 $\mu\text{m}$  beneath the interrogated surface. (b1-b3) Amplitude images from 300 $\mu\text{m}$  hole obtained from LIT demodulation at camera frame rates of 9 fps, 15 fps and 33, respectively. (c1-c3) represent similar images from 500 $\mu\text{m}$  hole and (d1-d3) from 800 $\mu\text{m}$  hole. The dotted circle in each image represent the true size of the hole. Mean normalized intensity of the pixels inside the hole at different frame rates from 300 $\mu\text{m}$  (b4), 500 $\mu\text{m}$  (c4), and 800 $\mu\text{m}$  (d4) holes. The error bar indicates the STD of the pixels inside the hole. Table (e) depicts mean  $\pm$  STD of MSRs and CNRs and the averaged NRMSD. The STDs in MSR and CNR were calculated from the 3 repeated measurements on the same hole at the same frame rate. MSRs and CNRs were calculated from the background (red rectangle in (b1)) and the foreground regions (black rectangle in (b1)) from all images.

**Low-cost LIT system for the detection of early dental caries.** Dental caries remains the most prevalent chronic disease in both children and adults worldwide [32-34]. Detection of dental caries at early stages is of prime importance in Dentistry as the progression of caries can be stopped (or even reversed) only at early stages [35-36]. However, existing clinical methods in Dentistry (X-ray and Visual/Tactile Inspection) do not have sufficient sensitivity to detect early stages of tooth demineralization [37]. Our research results with research-grade LIT systems [18-19] demonstrate the possibility of detecting caries at early stages, but the cost and size of LIT systems have always posed a barrier to translation of this technology to Dentistry. To demonstrate the possibility of performing detection of early caries using a low-cost and size LIT system, we carried out detection experiments on extracted human teeth with artificially induced early caries. A demineralization gel was prepared (detailed in method section) to induce caries in a controlled manner on healthy extracted teeth. This gel mimics the properties of bacterial plaques on enamel, providing an environment for the cyclic occurrence of demineralization and remineralization and thus the creation of early caries [30]. For the sample reported in this manuscript, two treatment windows were created on the tooth by exposing the left and right treatment windows to the gel for 3 and 7 days, respectively.

The visual photograph of the sample after artificial demineralization is shown in Figure 4.4 (a); red rectangles depict the locations of the two treatment windows. The size of the demineralization windows was approximately equal to 1mmx2mm and the distance between two windows was ~1.5mm. While visual inspection of the sample after demineralization could not detect any colorimetric abnormalities/white spot lesions, the presence of demineralization is clearly detected by the developed low-cost LIT system in both amplitude and phase images obtained at a modulation frequency of 2 Hz, Figure 4.4 (b)-(c). In the amplitude image, Figure 4.4 (b), a higher intensity of demineralized region is due to the enhancement in local absorption of laser illumination by demineralization by-products; thus, generating a thermal wave of higher amplitude compared to the surrounding intact areas [38]. The treatment windows are seen as areas of different contrast in the phase image as well, Figure 4.4(c). This is because the enhancement of light absorption in caries region shifts the local centroid of the thermal wave field, causing a phase shift in the thermal signals compared to those of the surrounding intact areas.

In order to quantify the diagnostic performances of our low-cost LIT system for detecting early dental caries, the contrast value of pixels inside the treated windows was compared to those of the healthy region. Figure 4.4(d) shows the segmented healthy, 3 days demineralization and 7 days demineralization areas of the amplitude image, panel (b). The pixel values of the treated windows were considerably higher than the average pixel value of the whole image; therefore, they can be reliably segmented from the intact surfaces by simple thresholding. After thresholding, means and STDs of the pixels inside the healthy and treated windows were calculated and compared. Figure 4.4(e) and 4.4(f) show the average intensity of the healthy, 3 days demineralization and 7 days demineralization windows from the amplitude and phase image, respectively. The error bars on bar plots indicate mean  $\pm$  STD. The average intensities of the treatment windows are considerably higher than that of the healthy region. There was no overlap between the error bars of healthy and 3 days demineralization window in both amplitudes and phase images, indicating a qualitative difference between the mean values. Although the error bars of 3 days and 7 days treated windows are overlapped, the mean amplitude and phase values of 7 days demineralization window are higher than those of 3 days demineralization window suggesting the presence of more advanced caries in the 7-day demineralization window. The results of the study are consistent with our previous LIT studies of early dental caries with high-end research-grade IR cameras [18-19] that also show increased contrast in the amplitude and phase images at caries sites compared to the healthy areas.

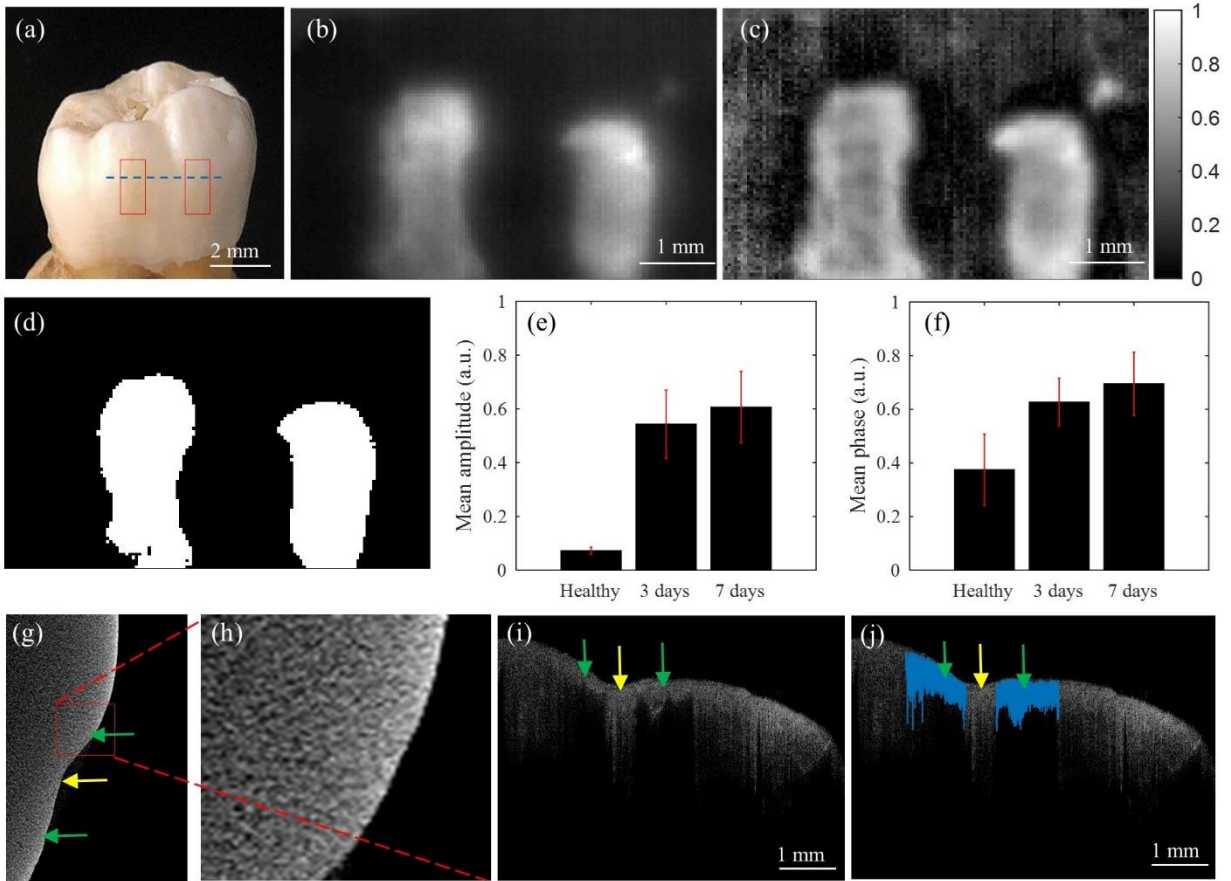


Figure 4.4. (a) A visual photograph of a dental sample; left and right treatment windows were demineralized for 3 and 7 days, respectively. LIT (b) Amplitude and (c) phase images obtained at 2Hz modulation frequency. (d) segmented demineralized windows. (e) Mean amplitude and STD from the healthy and demineralized areas shown in (d). (f) Mean phase and STD from the healthy and demineralized area shown in (d). (g)  $\mu$ CT slice taken of treatment windows (green arrows). (h) Zoomed area of a treatment window (i) OCT B-scan was taken from the treatment windows along the dashed line in (a). (j) Segmented demineralization areas in blue; average OCT penetration depths: 180  $\mu$ m for 3 days and 163  $\mu$ m for 7 days; average OCT intensities:  $49.52 \pm 27.90$ dB for 3 days and  $54.68 \pm 29.50$ dB for 7 days.

Figure 4.4(g) depicts a Micro-Computed Tomography ( $\mu$ CT) slice of the sample taken along the dashed line indicated in Figure 4.4(a). Due to the small extent of demineralization and inferior sensitivity of X-ray to demineralization,  $\mu$ CT is unable to detect the treatment window in both 3 days and 7 days of the demineralization periods. Fig. 4(h) is a magnified  $\mu$ CT image of a treatment window that is unable to show the material loss due to demineralization. Figure 4.4(i) shows the OCT B-scan taken from the healthy and treatment windows along the dashed line indicated in Figure 4.4(a). Here, the two treatment windows are clearly visible due to significant enhancement of light scattering at early caries sites and shadowing of deeper regions. The treatment windows in the OCT images were segmented, blue color in Figure 4.4(j), and the

average OCT penetration depth and intensity were calculated. OCT results suggest reasonably similar penetration depth for the two treatment windows (180  $\mu\text{m}$  for 3 days and 163  $\mu\text{m}$  for 7 days). Slightly less penetration depth of the 7-day treated window is due to the increase in light scattering due to additional demineralization compared to the 3-day treated window. The averaged OCT intensities of the two windows were also similar ( $49.52 \pm 27.90$  dB for 3 days and  $54.68 \pm 29.50$  dB for 7 days). The results of this study support previous findings that the optical scattering increases with mineral loss in artificially demineralized dental enamel [36]. The results of Fig. 4 demonstrate the ability of developed LIT system for detecting early stages of demineralization, which is at least 2 orders of magnitude lower in cost compared to the competing early caries detection technology of OCT.

**Low-cost LIT system for the detection and quantification of THC in oral fluid.** With recent changes in the legalization of cannabis around the world, there is an urgent need for rapid, yet sensitive, screening devices for testing drivers and employees under the influence of cannabis at roadside and workplace, respectively. To determine the viability of our technology for detecting THC (the principal psychoactive constituent of cannabis) at point-of-care, we conducted experiments with the commercially available saliva-based lateral flow immunoassay (LFA) test strips. A detailed description of LFA technology can be found elsewhere [39]; but, briefly, LFAs are simple paper-based devices used for the detection and quantification of analytes in a complex mixture. A developed LFA test strip shows two colored bands: the test and the control bands. The intensity of color at the test band correlates with the amount of target analyte (e.g., THC) present in the solution, while the presence of the control line ensures the validity of the experiment. In this LIT study, commercially available oral fluid LFA strips for detection of THC with a nominal detection limit of 25ng/ml were used. These LFAs were manufactured in a competitive format, in which an increase in THC concentration yield reduction of color intensity in the test band.

These LFAs were spiked at six different concentrations: 0, 2, 5, 7.5, 10 and 25 ng/ml. Eight LFAs were spiked at each concentration. LIT experiments on LFAs were performed at laser modulation frequencies of 2Hz. To test the repeatability, each LFA was imaged 5 times. Figure 4.5(a) shows a representative amplitude image of LFA strip spiked at 5 ng/ml of THC in oral fluid. The left and right lines depict the control and test band, respectively. These bands are

detected as areas of higher thermal wave amplitude because the immobilized gold nanoparticles (GNPs) at these sites efficiently absorb the laser excitation through surface plasmon resonance. To minimize the systematic errors induced by day-to-day variations in laser illumination system and manufacturing of LFAs, the contrast of LFA test strips in amplitude image were normalized with respect to those of the surrounding white nitrocellulose paper (red rectangle shown in Figure 4.5(a)). For quantitative analysis, the average intensity of pixels over all the rows in a strip was calculated. The aforementioned process yields a plot with two bell-shaped curves, representing the control and test bands as seen in Figure 4.5(b). A metric was defined by averaging the amplitude values within the full width at half maximum (FWHM) of the test band (between points A and B in Figure 4.5b). Throughout this paper, we will adopt this value as the amplitude metric. All quantitative analyses were carried out using this metric.

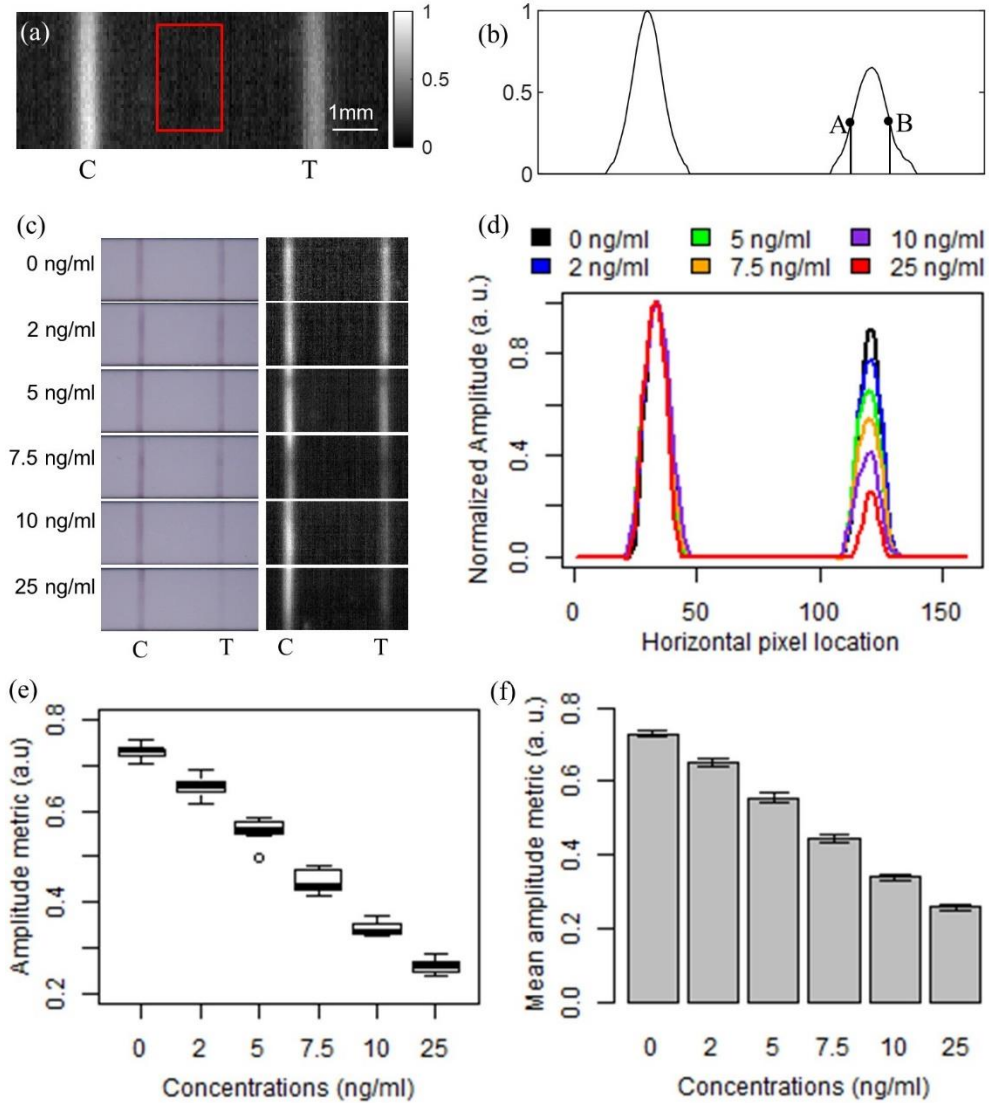


Figure 4.5(a) Representative LIT amplitude image of LFA spiked with 5ng/ml THC-saliva solution. (b) Two curves obtained at the control and test line by averaging the pixels in the vertical direction of (a). (c) Visual microscopy and LIT comparisons of representative LFAs at different concentrations. (d) Comparison of amplitude metric between panel (c) 6 representative LFAs at concentrations 0, 2, 5, 7.5, 10 and 25 ng/ml. (e) distribution of amplitude metric from all the LFAs at different concentrations (n=240). (f) Comparison of mean amplitude metric among different concentrations. The error bar shows the 99% confidence interval.

Figure 4.5(c) shows visual microscopy and LIT amplitude images of 6 representative LFAs at various THC concentrations. It can be seen that the decrease in the contrast at the test lines is associated with the increase in THC concentration in both visual and LIT images. However, the change of test line contrast with a decrease in THC concentration is more pronounced in LIT images, suggesting better detection sensitivity of LIT compared to visual interpretation. Figure 4.5 (d) shows the amplitude metrics obtained from the six LFAs shown in Figure 4.5(c);

the peak values of the test line curves show clear correlation with the concentration of THC. To verify enhanced detection performance of LIT over visual observation, the amplitude metrics were calculated for all LFA measurements. Figure 4.5(e) depicts the distribution of all the amplitude metrics (n=240: six concentrations × eight LFAs at each concentration × each LFA imaged five times). Each box displays the amplitude metric values of the LFAs of the same concentration (n=40: eight LFAs at each concentration × each LFA imaged five times). The box plot shows that there is no overlap in the distribution of data between any two concentration groups. The mean amplitude metrics with 99% confidence interval error bars are depicted in Figure 4.5(f), showing no overlap between the error bars of any two concentration groups. To compare mean amplitude metric values among different THC concentration groups, the one-way analysis of variance (ANOVA) was conducted. One-way ANOVA test showed statistically significant differences between the mean normalized amplitude values of different concentration groups ( $p < 0.001$ ). Tukey's honestly significant difference (Tukey's HSD) test was adopted to perform the pair-wise comparison. Tukey's pairwise comparisons showed that all the pairwise group comparisons were significantly different ( $p < 0.001$ ). Effect size of 0.97 and statistical power of 1.0 was obtained at a significance level of 0.01 and a sample size of 40 in each concentration group. The post-hoc pair-wise comparison illustrates that the developed low-cost LIT system can reliably differentiate LFAs spiked at 2 ng/ml concentrations from the 0 ng/ml, demonstrating suitability for enforcement of the 2ng/ml legal *per se* limit in many jurisdictions. Sensitivity, specificity, and accuracy of differentiating THC concentrations of 2 ng/ml and more from 0 ng/ml were found to be 95% that is considerably higher than the >80% standard set by Driving Under Influence of Drugs, Alcohol and Medicines (DRUID) for the nominal detection threshold of a drug screening device [40]. The data of Figure 4.5(f) can also be seen as calibration data through which THC concentration in saliva samples can be quantified.

The LFAs used in this study are low-cost solutions that are designed by the manufacturer to be interpreted visually. We recently conducted a human study to determine the limit of detection of visual interpretation of these LFAs; we also compared interpretations of human vision to those from a research-grade benchtop LIT system that incorporated an expensive (~\$10k) infrared camera [41]. The results of that study revealed detection limits of 10 ng/ml and 2 ng/ml for interpretation by human vision and research-grade benchtop LIT system, respectively. The results of Figure 4.5, as such, demonstrate that the low-cost LIT system described in this

manuscript provides comparable performance to that of high-end research grade LIT systems at fraction of the cost, paving the way for commercialization and widespread adoption of this AT technology.

The size (~15cm x 10cm x 8cm) and cost (~\$800) of our system are less than those of commercially-available oral fluid DRAGGER DRUG TEST 5000. Therefore, it has great potential for translation to roadside and workplace as a low-cost and portable testing device, while offering THC detection performance that aligns with DRUID expectations. In addition, the portable thermo-photonic reader is expected to offer lower consumable cost compared to the existing solutions as it utilizes commercially-available inexpensive (~\$8) colloidal gold nanoparticle-based LFAs.

#### **4.4. Conclusions**

AT is a widely used non-destructive testing technique for the detection of defects based on their radiometric thermal signatures. To date, AT has been utilized for interrogation of a broad spectrum of materials, spanning from the detection of manufacturing defects in industrial parts to the detection of diseases in biological specimens. However, despite the wide span of applications, the commercialization of AT technologies has long been impeded by the high cost and large size of the IR cameras used in this technology. In this manuscript, we report on the possibility of performing scientific and reliable AT using low-cost and size cellphone attachment IR cameras. Our results suggest that the developed SDK not only allows for on-demand control of camera attributes but also enables reliable and consistent acquisition of IR images at a high frame rate of 33 fps from a ~\$250 camera with a nominal frame rate of 9 fps. To demonstrate the impact of developed low-cost LIT systems, we present and discuss two high impact biomedical applications. Our results on the detection of early demineralization of human tooth clearly demonstrate the ability of the developed low-cost system in detecting early caries; thus, paving the way for translation of AT technologies to Dentistry as a preventive tool for alleviating the significant financial and societal burdens of dental caries on families, governments, and health care systems. Our demonstration of the possibility of measuring THC in oral fluid with the low-cost system, enables commercialization of a low-cost point-of-need portable device, for roadside

or workplace, for detecting and quantifying THC at an unprecedented low detection threshold of 2ng/ml; a task not achievable by any commercially available point-of-need devices in the market.

## 4.5. Methods

### 4.5.1. Principle of Lock-in Thermography (LIT)

The principle of LIT is based on the introduction of a periodically modulated light source on the surface of the sample and monitoring the resulting local surface temperature of the sample via an IR camera [4]. Absorption of modulated light excitation creates a modulated temperature field (aka thermal-wave field) inside the sample extending axially to a depth proportional to the thermal diffusion length [42]. In this configuration, the presence of defects alters the centroid of the induced thermal-wave field in the defective region, resulting in depth-integrated radiometric signals different from those registered in intact areas. The lock-in demodulation of the depth-integrated signals leads to the calculation of phase and amplitude images [6]. Since the intensity-modulation of excitation in LIT is carried out at a single frequency ( $f_m$ ), the LIT demodulation of temporal radiometric responses reveals the defective areas in both amplitude and phase images/channels [43]. The presence of subsurface defects, normally, results in an increase in amplitude values as the thermal impedance introduced by defects results in an additional diffusive thermal contribution to sample surface temperature. Defects also can be identified in phase images because of the alteration of the center of gravity of the thermal-wave field in the defective zone by the introduction of thermal impedance. While generally, amplitude images offer better SNR, LIT phase images are inherently emissivity-normalized and as such not prone to errors caused by variations in emissivity of sample surface [44]. Another key advantage of LIT is its depth profilometric nature. That is, inspection depth in LIT is controlled via the intensity-modulation frequency of external excitation,  $f_m$ , and in accordance with the definition of thermal diffusion length (i.e.,  $\mu = \sqrt{\alpha/\pi f_m}$  with  $\alpha$  as thermal diffusivity). As a result, probing deeper into the sample can be achieved by reducing the modulation frequency, while LIT inspection at high modulation frequencies is suitable for the detection of superficial defects (e.g., coatings defects).

**Development of the low-cost lock-in thermography system.** A schematic diagram of the LIT imaging system built in our lab using a low-cost cellphone attachment IR camera is shown in Figure 4.6a. A fiber-coupled (core diameter =200  $\mu\text{m}$ ), continuous-wave near-infrared laser with a center wavelength of 808 nm (Jenoptik, Jena, Germany) was used as an excitation light source. The intensity of excitation light was collimated and homogenized using a collimator and optical diffuser (Thorlabs, Newton, New Jersey, USA, F220SMA-780 and ED1-C20-MD). The sample was secured on a LEGO-jig and mounted on a 3-axis translation stage and excited by the light source. A multifunctional data acquisition unit (National Instruments, Austin, Texas, NI USB-6363 BNC) was used to modulate laser intensity at the desired modulation frequency ( $f_m$ ). The thermal responses of the sample were registered by using a low-cost cellphone attachment IR camera (SEEK THERMAL COMPACT; Seek Thermal Inc.; Android; 156 $\times$ 207 Pixels) in conjunction with a low-cost (~\$10) CO2 laser cutting Zinc Selenide objective lens ( $f = 1''$ ).

While the nominal frame rate of the camera through its standard applet is less than 9 fps, we have managed to utilize USB 2.0 documentation and Microsoft Windows native application programming interfaces (APIs, such as WinUSB and SetupAPI) in order to set up packets of information and send them to the camera's default endpoint address and, subsequently, acquire frame data from the camera through a corresponding pipe. As such, the developed platform has not only the ability to control camera attributes through a simple USB interface but also can achieve a stable high frame rate of 33 fps through a circular buffer hierarchy and multi-threading. In addition, the program controls the camera shutter and calibrates the camera before capturing the frames, providing stable frames up to a maximum frame rate of 33 fps after calibration. In order to compensate for the non-uniform sampling of data, in our previous work [29] we recorded timing information of each frame captured by the camera and employed spline interpolation at a uniform sampling frequency before applying LIT demodulation. The developed SDK, on the other hand, has the ability to capture frames at a constant frame rate, so interpolation is not necessary before the LIT demodulation of thermal signals.

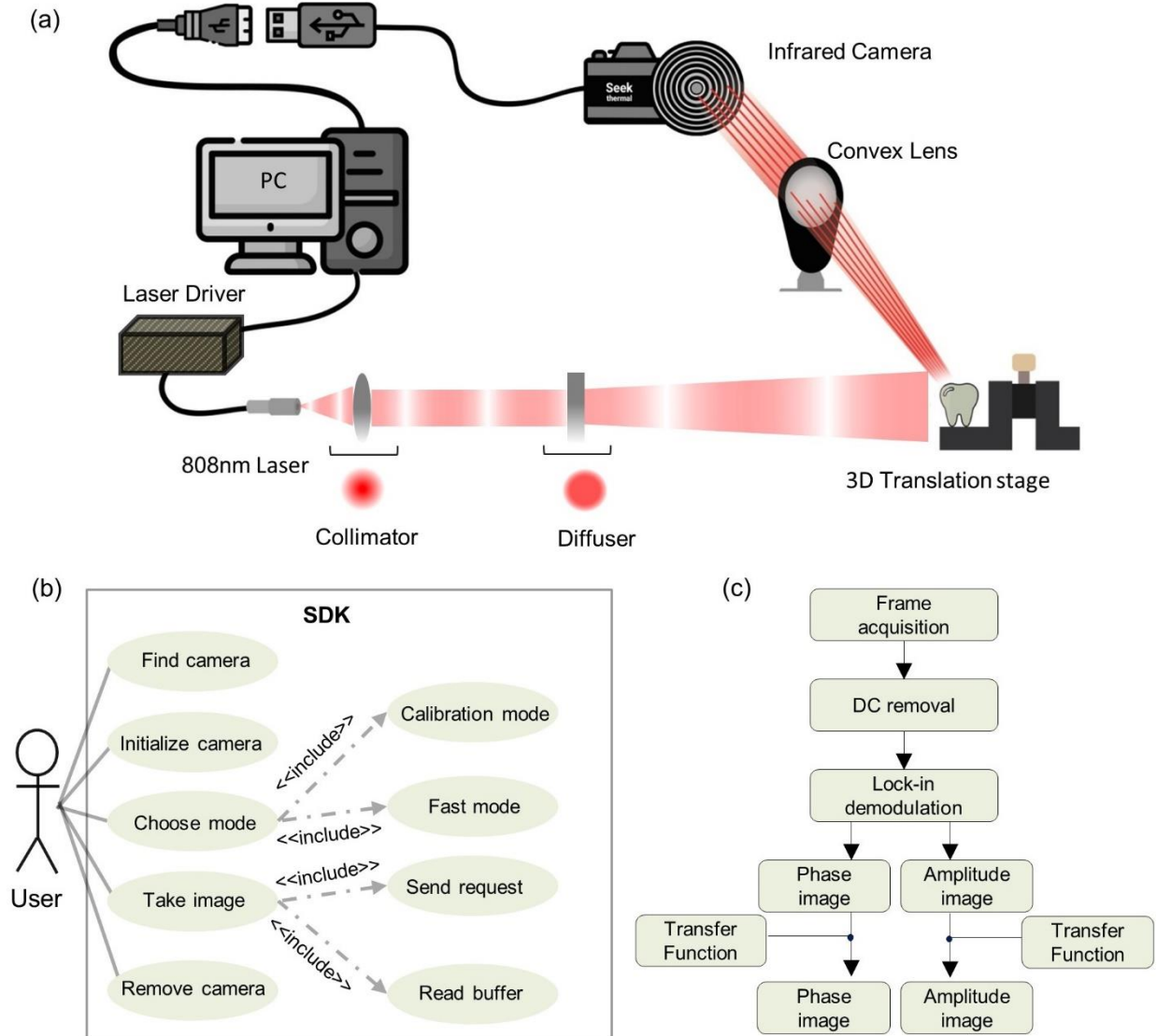


Figure 4.6. (a) Schematic diagram of the lock-in thermography system (b) A use case diagram that depicts a blueprint of the functionalities provided by our developed SDK. (c) A flow chart showing the signal processing method applied to the waveform at each pixel of the image

Figure 4.6b is a use case diagram that depicts a blueprint of the functionalities provided by our developed SDK for controlling the camera and capturing camera frames at a constant and uniform frame rate. First, the user initiates the SDK and checks if the IR camera is connected to the system. Then, the user adjusts the camera setting and initializes the camera for display and visualization of raw frames. Once these initialization processes are carried out, the SDK allows the system to take raw frames in two modes: calibration mode and fast mode. In the calibration mode, camera frames are captured while the shutter is closed and the camera's internal non-

uniformity correction map is recalibrated. The user can adjust the number of frames required for the calibration of the camera. Once the camera calibration is done, the system is set to take images in fast mode at the desired camera frame rate up to a maximum of 33 fps and without any disruption in the acquisition. Capturing frames in fast mode are carried out by sending a request for a frame acquisition followed by a read buffer command to move the acquired frame and time stamp information from camera memory. Once all images are captured, the camera is removed from the system and these captured frames are processed for LIT demodulation as described in Figure 4.6c.

Figure 4.6c depicts the signal processing steps applied to the temporal signal of each camera pixel for LIT demodulation. That is, after acquiring frames, first the effect of bulk heating is removed from the temporal signal by fitting a polynomial curve. After testing curves of different orders, we discovered a polynomial curve of order seven to be the optimum compromise between efficiency and required computation power. Then, a fast Fourier transform (FFT) is applied to the waveform, followed by determination of the magnitude and phase of the complex number corresponding to the laser modulation frequency in the Fourier domain. At last, the transfer function of the system is applied to the amplitude and phase images to correct imperfections caused by nonuniformities in the illumination and collection optical sub-systems. The transfer function was calculated by performing lock-in imaging on a thick Aluminum block painted with matt black paint on the front surface that resembles a semi-infinite blackbody sample. The theoretical amplitude and phase responses of such samples are known. Therefore, we found the experimental amplitude and phase images at desired modulation frequencies and then calculated the compensation factor for each camera pixel that once applied to the experimental pixel value, yield the theoretical prediction. With this practice, any systematic error caused by illumination and/or acquisition sub-systems can be compensated for. Once the amplitude and phase transfer functions at given modulation frequency are calculated based on the semi-infinite sample, they can directly be applied to amplitude and phase images of any sample to remove the effects of system systematic errors.

**Spectral-domain optical coherence tomography.** A spectral-domain OCT system that comprised of a 1315nm near-infrared superluminescent diode (Exalos; Switzerland) light source (maximum power 30mW) was used to take images of demineralized tooth. The OCT system is

based on Michelson interferometry in which 50/50 of light is split into the reference and sample arms by a fiber coupler. A polarization controller is used in the reference arm to adjust polarization to the cross-polarization state. A-line scan camera in the spectrometer was composed of 2048 pixels and could acquire A-lines up to a maximum scan/acquisition rate of 140 kHz. The theoretical axial and lateral resolution of the system in teeth is approximately 5  $\mu\text{m}$  and 10  $\mu\text{m}$ , respectively. A GPU (Graphics Processing Unit) based processing was developed for real-time display of OCT B-scans (i.e., cross-sectional image). The B-scan captured from the system were used for studying the effects of demineralization. To find the depth of caries using OCT images, the location of the surface where the scattering occurs and the location of the surface where the scattering ends is thresholded in each vertical line inside the demineralization windows. The color-coded areas in Fig. 3j indicate the thresholded area. Since the depth of each vertical line is unequal, average depth is reported as the depth of caries.

**Micro-computed Tomography.** Micro-Computed Tomography (SKYSCAN 1272 high-resolution  $\mu\text{CT}$  system, Bruker MicroCT, Kontich, Belgium) was used to take images of the demineralized teeth. The sample was placed in a LEGO block such that the treatment window would fall in the field of view of the  $\mu\text{CT}$  detector. A 0.5-mm Al/ 0.038-mm Cu filter was used to minimize the effects of beam hardening. The tooth was scanned at a rate of 87 kV with camera pixel size of 7.4  $\mu\text{m}$  and exposure time of 2000 ms per frame and a rotation angle of 0.1 degrees. The  $\mu\text{CT}$  images (n= 2813) were reconstructed from 1920 projections using NRECON software (Version 1.7.1.6., Skyscan, Kontich, Belgium).

**Aluminum Samples:** To examine acquisition disruptions and frame rate of manufacturer's applet and developed SDK (Fig. 1) LIT experiments were carried out on thick Aluminum block (40mm $\times$ 30mm $\times$ 30mm) with no internal defects. To test the advantage of a higher frame rate for better spatial resolution, an aluminum pin fin thermal heat sink sample was used (Fig 2a; Wakefield-Vette, New Hampshire, United States). The dimension of the heat sink is 40.6mm $\times$ 40.6 $\times$ 13.3mm and consists of pin fins of cross-section size 1.4mm $\times$ 2.4mm beneath the 2-mm thick plate, as shown in Fig. 2a. LIT experiments were conducted on plate surface of the thermal heat sink (area shown by the red dashed rectangle in Fig. 2a). The area imaged on the 156  $\times$  207 pixels of the camera was 7.43 $\times$ 9.86mm<sup>2</sup>, respectively. The spatial pixel size of images from the interrogated surface is, therefore,  $\sim$ 48 $\mu\text{m}$ . Raw frames were collected for 90 seconds

and those frames were demodulated according to lock-in principles to compute amplitude images. To study the subsurface defect (Fig. 3a), a custom-made Aluminium block (dimensions 45mm×25mm×30mm) was used. Three subsurface circular holes of diameter 5mm were created by drilling the block from the back side. The aforementioned simulates circular defects at 300µm, 500µm, and 800µm below the intact interrogation surface. The thermal diffusivity and conductivity of the aluminum were  $9.1 \times 10^{-5} \text{ m}^2/\text{s}$  [45] and 205 W/mK [46], respectively. In all LIT experiments carried out on aluminium samples the average optical intensity on the sample surface was  $1.6 \text{ W}/\text{cm}^2$  and temporal temperature responses were recorded for 60 seconds.

**Dental sample:** The anonymous human teeth were collected from local oral surgeons and in accordance to the bio- and laser safety guidelines in place at York University. These specimens were stored in distilled water inside the fume hood to prevent dehydration. In order to induce demineralization in specimens in a controlled manner, an acidified gel was prepared by mixing 0.100 M lactic acid and 0.100 M sodium hydroxide to give a pH value of 4.5 and then adding 6% w/v hydroxyethyl cellulose [18-19].

A tooth with no visible defect or white spot lesion was selected, rinsed thoroughly with distilled water and dried in the air before exposure to the demineralizing gel. In order to achieve localized demineralization, the surface of the tooth was covered by transparent nail polish, leaving small windows (aka treatment windows) exposed. The sample was then submerged upside down in a test tube containing 25 ml of acidified gel for specified durations of demineralization. Two treatment windows were created on the tooth by exposing the left and right treatment windows to the gel for 3 and 7 days, respectively. At the conclusion of artificial demineralization, the sample was removed from the test tube, rinsed under running water, nail polish was removed using Acetone and rinsed again with water before conducting LIT imaging. To take LIT images of the dental sample, the cellphone attachment camera was focused on the surface of the sample that is securely mounted on a LEGO block. LIT imaging was carried out on dental sample by recording the thermal responses for 30 seconds at modulation frequency of 2Hz. The average optical intensity on the sample surface was  $1 \text{ W}/\text{cm}^2$ .

OCT imaging was conducted at scan/acquisition rate of 100 KHz. Polarization controller in reference arm was adjusted to the cross-polarization state to minimize surface reflections. To segment the demineralized areas from the healthy area in B-mode images, mean and STD of the

amplitude image was calculated and a thresholding operation was applied to the entire image. The global threshold value was calculated by computing the average pixel plus one STD of all the pixels of the image.

**Preparation of oral fluid THC solution and LFA strips:** To spike LFAs at different THC concentration, saliva samples containing  $\Delta^9$ -THC was prepared by adding known volumes of  $\Delta^9$ -THC stock solution (MilliporeSigma; Oakville, Canada) to non-stabilized artificial saliva (Pickering Laboratories, Inc, Mountain View, California, USA). The THC solution was prepared following the standardized procedure suggested by the Canadian Society of Forensic Science Drugs and Driving Committee was followed [47]. Commercially available oral fluid LFA strips (NARCOCHECK Saliva Test Strips, Kappa City Biotech SAS, Montluçon, France) were used. Six different concentrations (25, 10, 7.5, 5, 2 and 0 ng/ml) of THC-saliva solution was prepared. In each experiment, 150  $\mu$ L of the solution was pipetted to the sample pad of the LFA strip. Eight LFAs were spiked at each concentration to investigate reproducibility and each LFA was interrogated five times using the developed low-cost LIT system to investigate repeatability. All LIT experiments were carried out with average optical intensity of 1.6 W/cm<sup>2</sup> and temporal temperature responses were recorded for 60 seconds.

**Data Analysis:** The SNRs of waveforms from our developed SDK and manufactures applet was calculated from the time signals spectra using the following Fourier-domain definition:

$$SNR = 20 \log_{10}(A_s/A_n) \quad (4.5.1)$$

Here,  $A_s$  is the amplitude of the signal at the applied modulation frequency of 1Hz and  $A_n$  is the average amplitude of the noise in the region depicted in Figs. 1c and 1d. For the calculation of SNR, an average amplitude of noise was calculated from the frequency range of 0.2Hz to 0.8Hz, (regions shown by the red dashed rectangles in Figure 1c and 1d).

The root-mean-square deviation (RMSD) and the normalized RMSD are defined as [48]

$$RMSD = \sqrt{\frac{\sum_{i=1}^n (x_i - \bar{x}_i)^2}{n}} \quad \& \quad NRMSD = \frac{RMSD}{\bar{x}_i} \quad (4.5.2)$$

where  $x_i$  is the intensity of a pixel in an experiment and  $\bar{x}_i$  is the mean intensity of  $n$  repeated experiments for  $i^{\text{th}}$  pixel. The NRMSD was calculated for each LIT image at each frame rate.

MSR and CNR were calculated using following definition [49]:

$$CNR = \frac{|\bar{\mu}_f - \bar{\mu}_b|}{\sqrt{0.5(\sigma_f^2 + \sigma_b^2)}} \quad \& \quad MSR = \frac{\bar{\mu}_f}{\sigma_f} \quad (4.5.3)$$

where  $\bar{\mu}_f$  and  $\sigma_f$  are the mean and STD of the foreground/defect region, and  $\bar{\mu}_b$  and  $\sigma_b$  are the mean and STD of the background region. The selected areas as foreground and background regions are shown in Fig. 3 (b1) by black and red rectangles, respectively.

#### 4.6. Supplementary Documents

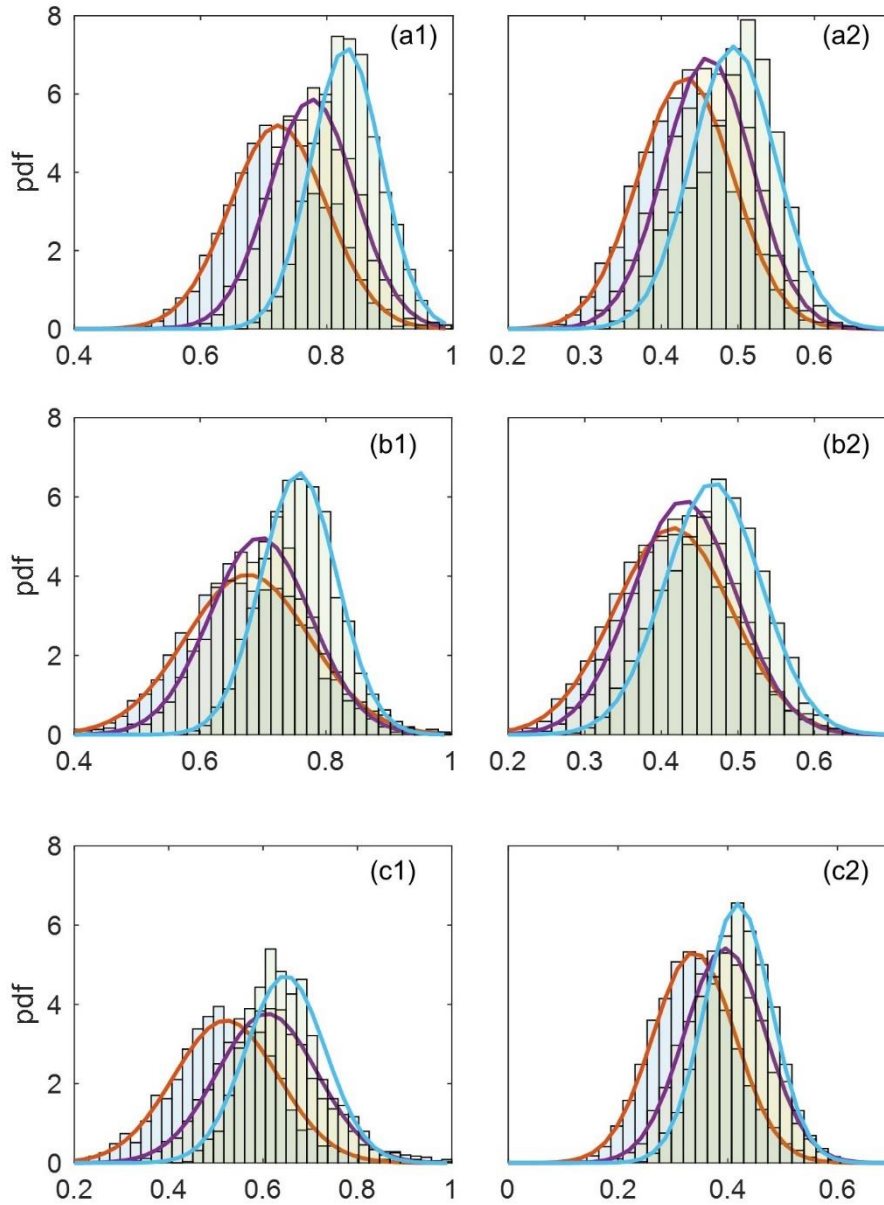


Figure 4.7. Histograms with probability density function (pdf) of the images at the foreground (left) and background region (right) at camera frame rates of 9, 15 and 33 fps for defects at different depths. The panel a, b and c are corresponding to defects 300μm, 500μm and 800μm below intact interrogation surface, respectively. Mean  $\pm$  STD of the pdf are reported in supplementary table 1.

Depth	Foreground			Background		
	9fps	15 fps	33 fps	9fps	15 fps	33 fps
300μm	0.7230 $\pm$ 0.0767	0.7767 $\pm$ 0.0680	0.8308 $\pm$ 0.0556	0.4318 $\pm$ 0.0621	0.4612 $\pm$ 0.0575	0.4941 $\pm$ 0.0553
500μm	0.6758 $\pm$ 0.0988	0.6956 $\pm$ 0.0802	0.7572 $\pm$ 0.0604	0.4153 $\pm$ 0.0765	0.4295 $\pm$ 0.0675	0.4674 $\pm$ 0.0627
800μm	0.5215 $\pm$ 0.1109	0.6086 $\pm$ 0.1060	0.6476 $\pm$ 0.0845	0.3388 $\pm$ 0.0751	0.3950 $\pm$ 0.0737	0.4186 $\pm$ 0.0610

Table 4.1 Means and STDs of the probability density functions calculated from the Supplementary Fig. 4.7.

#### 4.7. References

1. Almond, D. P. & Patel, P. M. *Photothermal Science and Techniques* (Chapman and Hall, London, 1996).
2. Tabatabaei, N. Matched-filter thermography. *Appl. Sci.* **8**(4), 581 (2018).
3. Moropoulou, A. I. & Labropoulos, K. C. Non-destructive testing for accessing structural damage and interventions effectiveness for built culture heritage protection, *Human-Computer Interaction: Concepts, Methodologies, Tools, and Applications*, Information resources management association USA (2015)
4. Huth, S. T., Breitenstein, O., Huber, A., Dantz, D., Lambert, U., & Altmann, F. Lock-in IR-thermography-A novel tool for material and device characterization. In *diffusion and defect data part B solid state phenomena*, 741-746 (2002).
5. Bates, D., Smith, G., Lu, D., & Hewitt, J. Rapid thermal non-destructive testing of aircraft components. *Compos. B. Eng.* **31**,175-85 (2000).
6. Ciampa, F., Mahmoodi, P., Pinto, F., & Meo, M. Recent advances in active infrared thermography for non-destructive testing of aerospace components. *Sensors.* **18**, 609 (2018).
7. Tabatabaei, N., & Mandelis, A. Thermal-wave radar: A novel subsurface imaging modality with extended depth-resolution dynamic range. *Rev. Sci. Instrum.* **80**(3), 034902 (2009)
8. Tabatabaei, N., Mandelis, A., & Amaechi, B. T. Thermophotonic radar imaging: An emissivity-normalized modality with advantages over phase lock-in thermography. *Appl. Phys. Lett.* **98**, 163706 (2011).
9. Tabatabaei, N. & Mandelis, A. Thermal coherence tomography using match filter binary phase coded diffusion waves. *Phys. Rev. Lett.* **107**, 165901 (2011).
10. Kaipilavil S., & Mandelis, A. Truncated-correlation photothermal coherence tomography for deep subsurface analysis. *Nat. Photon.* **8**, 635-642 (2014).
11. Tavakolian, P., Sivagurunathan, K., & Mandelis, A. Enhanced truncated correlation photothermal coherence tomography with application to deep subsurface defect imaging and 3-dimensional reconstructions. *J. Appl. Phys.* **122**, 023103 (2017).
12. Breitenstein, O., Warta, W., & Langenkamp, M. *Lock-In Thermography*. (Springer: Berlin, Germany, 2003).
13. Jäckel, P., & Netzelmann, U. The influence of external magnetic fields on crack contrast in magnetic steel detected by induction thermography. *Quant. Infrared Thermogr. J.* **10**, 237-247 (2013).
14. Krstulovic-Opara, L., Klarin, B., Neves, P., & Domazet, Z. Thermal imaging and thermoelastic stress analysis of impact damage of composite materials. *Eng. Fail. Anal.* **18**, 713-719 (2011).
15. Mendioroz, A., Celorrio, R., & Salazar, A. Ultrasound excited thermography: An efficient tool for the characterization of vertical cracks. *Meas. Sci. Technol.* **28**, 112001 (2017).

16. Wu, D., Salerno, A., Malter, U., Aoki, R., Kochendörfer, R., Kächele, P., Woithe, K., Pfister, K., & Busse, G. Inspection of aircraft structural components using lock-in thermography. *Quant. Infrared Thermogr. QIRT*, **96**, 251-256 (1996).
17. Ojaghi, A., Parkhimchyk, A., & Tabatabaei, N., First step toward translation of thermophotonic lock-in imaging to dentistry as an early caries detection technology, *J. Biomed. Opt.* **21**, 096003 (2016).
18. Tabatabaei, N., Mandelis, A., & Amaechi, B. T. Thermophotonic lock-in imaging of early demineralized and carious lesions in human teeth, *J. Biomed. Opt.* **16**, 071402 (2011).
19. Tabatabaei, N., Mandelis, A., Dehghany, M., Michaelian, K. H., & Amaechi, B. T. On the sensitivity of thermophotonic lock-in imaging and polarized Raman spectroscopy to early dental caries diagnosis. *SPIE* (2012).
20. Breitenstein, O., Langenkamp, M., Altmann, F., Katzer, D., Lindner, A., & Eggers, H. Microscopic lock-in thermography investigation of leakage sites in integrated circuits. *Rev. Sci. Instrum.* **71**, 4155–4160 (2000).
21. Cheng, L., & Tian, G.Y. Surface crack detection for carbon fiber reinforced plastic (CFRP) materials using pulsed Eddy current thermography. *IEEE Sens. J.* **11**, 3261-3268 (2011).
22. Zweschper, T., Dillenz, A., & Busse, G. Ultrasound lock-in thermography- a defect-selective NDT method for the inspection of aerospace components. *Insight* (2001).
23. Bonmarin, M., & Le Gal, F. A. Lock-in thermal imaging for the early-stage detection of cutaneous melanoma: a feasibility study, *Comput. Biol. Med.* **47**, 36-43 (2014).
24. Kaipilavil, S., Mandelis, A., Wang, X., & Feng, T. Photothermal tomography for the functional and structural evaluation, and early mineral loss monitoring in bones. *Biomed. Opt. Express.* **5**(8), 2488-2502 (2014).
25. Zhang, H., Tavakolian, P., Sivagurunathan, K., Mandelis, A., Shi, W., & Liu, F. F. Truncated-correlation photothermal coherence tomography derivative imaging modality for small animal in vivo early tumor detection. *Opt. Lett.* **44**(3), 675-678 (2019).
26. Rogalski, A. *Infrared detectors* (CRC press, 2010).
27. Rogalski, A. Infrared detectors: an overview, *Infrared Phys. Technol*, **43**, 187-210 (2002).
28. Wolfe, W. L., Kruse, P. W. & Bass, M. Thermal detectors. (OSA hand book of optics 1, 1995).
29. Razani, M. Parkhimchyk, A., & Tabatabaei, N. Lock-in thermography using a cellphone attachment infrared camera, *AIP Adv.* **8**, 035305 (2018).
30. Tabatabaei, N., & Mandelis, A. Thermal coherence tomography: Depth-resolved imaging in parabolic diffusion-wave fields using the thermal-wave radar. *Int. J. Thermophys.*, **33**(10-11), 1989-1995 (2012).
31. Shokouhi, E. B., Razani, M., Gupta, A., & Tabatabaei, N. Comparative study on the detection of early dental caries using thermo-photonic lock-in imaging and optical coherence tomography, *Biomed. Opt. Express.* **9**, 3983-97 (2018).
32. Department of Health and Human Services, Oral health in America: a report of the Surgeon General, NIH publication, 155-88 (2000).
33. Benjamin, R. M. Oral health: the silent epidemic, *Public health reports.*125, 158 (2010).

34. Abanto, J., Carvalho, T. S., Mendes, F. M., Wanderley, M. T., Bönecker, M., & Raggio, D. P. Impact of oral diseases and disorders on oral health-related quality of life of preschool children. *Community Dent. Oral Epidemiol*, **39**, 105-14 (2011).
35. Darling, C. L., Huynh, G., & Fried, D. Light scattering properties of natural and artificially demineralized dental enamel at 1310 nm. *J. Biomed. Opt.* **11**, 034023 (2006).
36. Dirks, O. B. Post-eruptive changes in dental enamel, *J. Dent. Res.* **45**, 503-11 (1966).
37. Alfano, M. C. National Institutes of Health Consensus Development Conference statement. Diagnosis and management of dental caries throughout Life. *J. Am. Dent. Assoc.* **132**, 1153-1161 (2001).
38. Matvienko, A., Mandelis, A., Jeon, R.J., & Abrams, S. H. Theoretical analysis of coupled diffuse-photon-density and thermal-wave field depth profiles photothermally generated in layered turbid dental structures. *J. Appl. Phys.* **105**, 102022 (2009).
39. Koczula, K. M., & Gallotta, A. Lateral flow assays. *Essays Biochem.* **60**, 111-20 (2016).
40. Schulze, H., Schumacher, M., Urmeew, R., Alvarez, J., Bernhoft, I. M., et al. Driving under the influence of drugs, alcohol and medicines in Europe-findings from the DRUID project, Lisbon: EMCDDA (2012).
41. Thapa, D., Samadi, N., Patel, N., & Tabatabaei, N. Thermographic detection and quantification of THC in oral fluid at unprecedented low concentrations. *Biomed. Opt. Express.* **11**(4), 2178-2190 (2020).
42. Ojaghi, A., Parkhimchyk, A., & Tabatabaei, N. Long-wave infrared thermophotonic imaging of demineralization in dental Hard tissue. *Int. J. Thermophys.* **37**(2016).
43. Pickering, S., & Almond, D. Matched excitation energy comparison of the pulse and lock-in thermography NDE techniques. *Ndt & E International.* **41**, 501-9 (2008).
44. Busse, G. & Eyerer, P. Thermal wave remote and non-destructive inspection of polymers. *Appl. Phys. Lett.* **43**, 355-7 (1983).
45. Dante, R. C. Handbook of friction materials and their applications. Chapter 9, Pages 123-134, (2016), Woodhead Publishing.
46. Young, High D. University Physics, 7<sup>th</sup> Ed., Chapter 15, Addison Wesley, 1992.
47. Canadian Society of Forensic Science Drugs and Driving Committee (DDC) Drug Screening Equipment-Oral Fluid Standards and Evaluation Procedures.
48. Kabsch, W. A solution for the best rotation to relate two sets of vectors. *Acta Crystallographica Section A: Crystal Physics, Diffraction, Theoretical and General Crystallography*, **32**(5), 922-923(1976).
49. Thapa, D., Raahemifar, K., & Lakshminarayanan, V. Reduction of speckle noise from optical coherence tomography images using multi-frame weighted nuclear norm minimization method. *J. Mod. Opt.* **62**, 1856-64 (2015).



# CHAPTER FIVE

## Conclusion and Future Work

### 5.1. Conclusion

Active thermography is non-contact method for non-destructive testing (NDT) of materials that is widely used in both defect detection in industry and disease detection in biology. Among different methods in active thermography, Lock-in thermography imaging (LIT) has shown best trade-off between system cost/complexity and detection performance. Despite promising applications of LIT in industry and medicine, commercialization and wide-spread adaption of LIT has long been impeded by the cost (usually \$10k-\$100k) and size of infrared cameras. In order to overcome these limitations, in this thesis, we aimed to demonstrate feasibility of performing LIT with cell-phone attachment infrared cameras with cost of ~\$250 and size significantly less than the research-grade infrared cameras.

In order to assess the ability of developed system in detecting internal defects in manufactured parts, we performed tests on an aluminum block sample with blind holes at three different depths. Results showed that not only our system can detect defects, but also it can distinguish between holes with different depths. In terms of higher impact applications, we tested our system for detecting THC in oral fluid and detecting early dental carries.

Detection of THC in oral fluid: Following the legalization of cannabis in Canada, the need of urgent rapid and sensitive test for roadside drivers check increased. One of the most commonly tests used in drug abuse screening is Lateral Flow immunoassays (mostly referred to as LFA). LFA, however, lack the needed precision in detecting THC (a principal psychoactive constituent of cannabis). The lowest threshold achieved using LFAs are normally limited to 25 ng/ml. This is limiting since this threshold is well above the *per se* limits set by many countries (usually 1 to 5 ng/ml) in order to define impairment, especially with respect to operating motor vehicles. To address this issue, we developed a low-cost portable thermo-phonic imager which offers highly sensitive detection and quantification of THC with detection cut off-limits as low as 2 ng/mL by

interrogating the thermal responses of gold nanoparticles (GNP) in LFA through active thermography platform. This low-cost and portable thermo-phonic imager promises an affordable solution which allows for proper enforcement of *per se* regulations worldwide. The developed technology can also be adapted for very sensitive detection of other analytes in GNP-based LFA platforms that are widely used in healthcare (e.g., COVID-19 Antibody LFAs) as well as food/water and workplace safety applications.

Detecting Early Dental Caries: As mentioned above, we also tested our system's ability to detect early dental carries. Dental carries are the main cause of tooth loss in all ages and one of the most chronic diseases among children which are preventable if detected in early stages. Current systems such as X-ray can detect the cavities with reasonable depth, so there is a need for low cost devices for this purpose. Our results showed that our system can detect the carries even as early as three days of demineralization. We also demonstrated that our system is capable to distinguish between two carries in different stages of demineralization (three and seven days).

Above studies indicate that our developed system has sufficient sensitivity to provide comparable performance to that of high-end research grade LIT systems at fraction of the cost, paving the way for commercialization and widespread adoption of this AT technology.

## **5.2. Future Work**

### **LIT Analyses of LFAs**

As part of the commercialization process of our handheld device for screening THC concentration in roadside and workplace, I have secured Lab2Market-Canada's research commercialization program grant (commencing September 2020). LAB2Market aims to provide researchers at universities across Canada guidance on how to commercialize their technologies and provides them with the required entrepreneurial skills. This will significantly help us with starting a spin off company and successfully commercializing our handheld device.

In light of recent COVID-19 outbreak, public health authorities around the world are looking for developing new ways to identify/test COVID-19 that are cheaper, faster and widely accessible. As such, we are exploring to adapt our technology to COVID-19 LFAs for early detection and

quantification of COVID-19 antibodies. Potential use cases of this innovation include but not limited to:

- Helping the Ontario health network with rapid and on-site detection of COVID-19 antibodies at early stages of disease at large scale
- Estimating degree of vulnerability in population so that appropriate recovery measures and policies can be designed and implemented by health authorities
- Identifying convalescent plasma with abundant antibody titers in blood donor clinics
- Providing employers with a more objective return-to-work screening which in return lowers the impact of the outbreak
- Helping researchers for development of vaccine and therapeutics strategies.

### **Detecting Early Dental Caries**

We are currently pursuing the development of a dental handheld imager using the low-cost cellphone attachment camera. We plan to perform ex-vivo validation studies with this handheld device on dental matrices and possibly artificial mouth system. We anticipate that further development of this low-cost AT system can significantly lower the cost of AT and hence paving the way for the translation of AT techniques to the clinical applications. The low-cost examination of teeth can benefit patients in rural areas and underdeveloped countries to reduce health care disparities.

## 6. References

1. Wigganhauser, H., *Active IR-applications in civil engineering*. Infrared Physics & Technology, 2002. **43**(3-5): p. 233-238.
2. Breitenstein, O., et al., *Microscopic lock-in thermography investigation of leakage sites in integrated circuits*. Review of scientific instruments, 2000. **71**(11): p. 4155-4160.
3. Ciampa, F., et al., *Recent advances in active infrared thermography for non-destructive testing of aerospace components*. Sensors, 2018. **18**(2): p. 609.
4. Kaczmarek, M. and A. Nowakowski, *Active IR-thermal imaging in medicine*. Journal of Nondestructive Evaluation, 2016. **35**(1): p. 19.
5. Wiecek, B. and S. Zwolenik. *Thermal wave method-limits and potentialities of active thermography in biology and medicine*. in *Proceedings of the Second Joint 24th Annual Conference and the Annual Fall Meeting of the Biomedical Engineering Society*[[Engineering in Medicine and Biology. 2002. IEEE.
6. Kaczmarek, M., et al. *Investigation of skin burns basing on active thermography*. in *2001 Conference Proceedings of the 23rd Annual International Conference of the IEEE Engineering in Medicine and Biology Society*. 2001. IEEE.
7. Tabatabaei, N., et al., *On the sensitivity of thermophotonic lock-in imaging and polarized Raman spectroscopy to early dental caries diagnosis*. Journal of biomedical optics, 2012. **17**(2): p. 025002.
8. Ibarra-Castanedo, C., et al., *Comparative study of active thermography techniques for the nondestructive evaluation of honeycomb structures*. Research in Nondestructive Evaluation, 2009. **20**(1): p. 1-31.
9. Genest, M., et al., *Pulsed thermography for non-destructive evaluation and damage growth monitoring of bonded repairs*. Composite Structures, 2009. **88**(1): p. 112-120.
10. Ibarra-Castanedo, C., et al., *Qualitative and quantitative assessment of aerospace structures by pulsed thermography*. Nondestructive Testing and Evaluation, 2007. **22**(2-3): p. 199-215.
11. Busse, G., *Nondestructive evaluation of polymer materials*. NDT & E International, 1994. **27**(5): p. 253-262.
12. Stoessel, R., et al. *Review of some measurement techniques involved in modern NDE*. in *Proceedings of the 4th International Workshop on Advances in Signal Processing for NDE*. 2001.
13. Vavilov, V.P. and S. Marinetti, *Pulsed phase thermography and fourier-analysis thermal tomography*. Russian Journal of Nondestructive Testing, 1999. **35**(2): p. 134-145.
14. BuSse, G., D. Wu, and W. Karpen, *Thermal wave imaging with phase sensitive modulated thermography*. Journal of Applied Physics, 1992. **71**(8): p. 3962-3965.
15. Galmiche, F. and X. Maldague. *Depth defect retrieval using the wavelet pulsed phased thermography*. in *Proc. QIRT*. 2000.
16. Maldague, X. and S. Marinetti, *Pulse phase infrared thermography*. Journal of applied physics, 1996. **79**(5): p. 2694-2698.
17. Tabatabaei, N., *Matched-Filter Thermography*. Applied Sciences, 2018. **8**(4): p. 581.
18. Tabatabaei, N. and A. Mandelis, *Thermal-wave radar: a novel subsurface imaging modality with extended depth-resolution dynamic range*. Rev Sci Instrum, 2009. **80**(3): p. 034902.

19. Tabatabaei, N., A. Mandelis, and B.T. Amaechi, *Thermophotonic radar imaging: An emissivity-normalized modality with advantages over phase lock-in thermography*. Applied Physics Letters, 2011. **98**(16): p. 163706.
20. Tabatabaei, N. and A. Mandelis, *Thermal coherence tomography using match filter binary phase coded diffusion waves*. Physical review letters, 2011. **107**(16): p. 165901.
21. Schlangen, R., et al. *Use of Lock-in thermography for nondestructive 3D defect localization on system in package and stacked-die technology*. in *proceedings of ISTFA*. 2011.
22. Breitenstein, O. and M. Langenkamp, *Lock-in thermography*. Advanced Microelectronics, Springer, Berlin, 2003.
23. Tabatabaei, N., A. Mandelis, and B.T. Amaechi, *Thermophotonic lock-in imaging of early demineralized and carious lesions in human teeth*. Journal of biomedical optics, 2011. **16**(7): p. 071402.
24. Meola, C., et al., *Non-destructive control of industrial materials by means of lock-in thermography*. Measurement Science and Technology, 2002. **13**(10): p. 1583.
25. Bonmarin, M. and F.-A. Le Gal, *Lock-in thermal imaging for the early-stage detection of cutaneous melanoma: a feasibility study*. Computers in biology and medicine, 2014. **47**: p. 36-43.
26. Karpen, W., et al. *Depth profiling of orientation in laminates with local lockin thermography*. in *Proc. QIRT*. 1994.
27. Meola, C. and G. Carlomagno, *The role of infrared thermography in NDT, in Nondestructive Testing of Materials and Structures*. 2013, Springer. p. 91-96.
28. An, Y.-K., J.M. Kim, and H. Sohn, *Laser lock-in thermography for detection of surface-breaking fatigue cracks on uncoated steel structures*. Ndt & E International, 2014. **65**: p. 54-63.
29. Swiderski, W. *Lock-in thermography for rapid evaluation of the destruction area in composite materials used in military applications*. in *Sixth International Conference on Quality Control by Artificial Vision*. 2003. International Society for Optics and Photonics.
30. John, C. and A. Salerno. *Raw data set of thermal wave propagation in hard dental tissues*. in *Proc. of 11th Int. Symp. and Exhibition for Computer Assisted Radiology (CAR97)*. 1997.
31. John, C., et al., *Applying phase sensitive modulated thermography to ground sections of a human tooth*, in *Nondestructive Characterization of Materials VIII*. 1998, Springer. p. 757-762.
32. Tabatabaei, N., et al., *On the sensitivity of thermophotonic lock-in imaging and polarized Raman spectroscopy to early dental caries diagnosis*. Vol. 17. 2012: SPIE. 1-5, 5.
33. Ojaghi, A., A. Parkhimchyk, and N. Tabatabaei, *First step toward translation of thermophotonic lock-in imaging to dentistry as an early caries detection technology*. J Biomed Opt, 2016. **21**(9): p. 96003.
34. Instruments, Z., *Principles of lock-in detection and the state of the art*. CH-8005 Zurich, Switzerland, Accessed, 2016.
35. Ojaghi, A., A. Parkhimchyk, and N. Tabatabaei, *First step toward translation of thermophotonic lock-in imaging to dentistry as an early caries detection technology*. Journal of biomedical optics, 2016. **21**(9): p. 096003.
36. Razani, M., A. Parkhimchyk, and N. Tabatabaei, *Lock-in thermography using a cellphone attachment infrared camera*. Aip Advances, 2018. **8**(3): p. 035305.

37. Shokouhi, E.B., et al., *Comparative study on the detection of early dental caries using thermo-photonic lock-in imaging and optical coherence tomography*. Biomedical optics express, 2018. **9**(9): p. 3983-3997.
38. Roopa, K.B., et al., *White spot lesions: A literature review*. Journal of Pediatric Dentistry, 2015. **3**(1): p. 1.
39. Hintze, H. and A. Wenzel, *Clinically undetected dental caries assessed by bitewing screening in children with little caries experience*. Dentomaxillofacial Radiology, 1994. **23**(1): p. 19-23.
40. Nyttun, R.B., M. Raadal, and I. Espelid, *Diagnosis of dentin involvement in occlusal caries based on visual and radiographic examination of the teeth*. European Journal of Oral Sciences, 1992. **100**(3): p. 144-148.
41. Tabatabaei, N. and A. Mandelis, *Thermal coherence tomography using match filter binary phase coded diffusion waves*. Phys Rev Lett, 2011. **107**(16): p. 165901.
42. Petersen, P.E., et al., *The global burden of oral diseases and risks to oral health*. Bulletin of the World Health Organization, 2005. **83**: p. 661-669.